Solar Irradiance Observed at Summit, Greenland: Possible Links to Magnetic Activity on Short Timescales

John E. Frederick

Department of the Geophysical Sciences, University of Chicago

5734 South Ellis Ave., Chicago, IL 60637 USA

E-mail: frederic@uchicago.edu

Corresponding Author: John E. Frederick

Abstract

Measurements of ground-level visible sunlight (400-600 nm) from Summit, Greenland over the period August 2004 through October 2014 define the attenuation provided by cloudiness, including its dependence on solar elevation and season. The long-term mean cloud-attenuation increases with increasing solar zenith angle, consistent with radiative transfer calculations which treat a cloud as a plane parallel layer with a strong bias toward forward scattering and an albedo for diffuse radiation near 0.1. The ratio of measured irradiance to clear-sky irradiance for solar zenith angles greater than 66^{o} has a small, but statistically significant, positive correlation with the previous day's magnetic activity as measured by the daily A_p index, but no clear relationship exists between the irradiance ratio and daily changes in the ground-level neutron flux measured at Thule over the time frame considered. A high value of A_p on one day tends to be followed by a day whose ground-level solar irradiance is slightly greater than would occur otherwise. In an average sense, the visible irradiance following a day with A_p>16 exceeds that following a day with $A_p \leq 16$ by 1.2-1.3% with a 95% confidence range of approximately ±1.0%. The results are broadly compatible with small changes in atmospheric scattering following magnetic disturbances.

Keywords: atmospheric opacity, high-latitude clouds, magnetic activity, solar irradiance, solar-terrestrial coupling

1. Introduction

The transmission of sunlight through the Earth's atmosphere is important in determining the surface energy balance at any location. In the visible part of the spectrum the atmosphere is relatively transparent, with contributions to opacity coming from scattering by molecules and particles and by liquid droplets or ice crystals in clouds. This work examines the transmission of visible solar radiation to the Earth's surface based on more than 10 years of measurements from Summit, a research station close to the apex of the Greenland ice sheet. An effort of special interest involves seeking links between atmospheric opacity and indices of magnetic activity.

Observational studies conducted over several decades have revealed links between measures of magnetic disturbance and the circulation of the lower atmosphere (Roberts and Olson, 1973; Wilcox et al., 1973), atmospheric transparency (Roldugin and Tinsley, 2004), and cloud properties (Svensmark and Friis-Christiansen, 1997), where potential mechanisms relate to atmospheric electricity or energetic particle precipitation (Tinsley et al., 1989). Tinsley (2008) provided a comprehensive review of research available as of 2008 and summarized processes that might be responsible for the observed couplings. The global electrical circuit, first proposed by Wilson (1920), could provide a link between magnetic variations and the lower atmosphere. The background electric field between the ionosphere and ground drives a downward current that may influence the microphysics of aerosols and clouds (Tinsley, 2008). Changes in the interplanetary magnetic field influence the potential difference between the ionosphere and ground and therefore the current that flows through the lower atmosphere (Tinsley et al., 2007; Tinsley, 2008). In this mechanism, a change in the vertical electric current is responsible for a magnetic activity-lower atmosphere coupling.

Another mechanism could involve changes in tropospheric ionization due to a varying cosmic ray background. These changes would perturb chemical processes that influence condensation nuclei and cloudiness (Dickinson, 1975; Svensmark et al., 2009; Kirkby et al., 2011; Almeida et al., 2013; Svensmark et al., 2013). Several analyses have advanced this hypothesis to explain observed links between cloud properties and magnetic disturbances (Kazil et al., 2006; Laken and Kniveton, 2011). While this chain of events is plausible, other studies have concluded that the effects of such solar-terrestrial couplings must be small (Laken et al., 2012; Sloan and Wolfendale, 2013). After a review of the available evidence, IPCC (2013) stated that, while weak correlations between cloudiness and cosmic radiation might appear in some locations, such couplings were not significant on the global scale.

The high geomagnetic latitude of Summit, about 76^{o}, makes it an interesting location at which to search for links between atmospheric opacity and magnetic activity. If a relationship between ground-level irradiance and magnetic activity indeed exists, it is likely weak and not straightforward to detect. Still, if the transmission properties of the high-latitude atmosphere respond to magnetic variations, even to a very small degree, this is an important result to establish using the dataset from Summit.

2. The Dataset and Calculations

The dataset used here was obtained by the Biospherical Instruments, Inc. SUV-150B scanning spectroradiometer located at Summit, Greenland, latitude $72^{o}35'$N, longitude $38^{o}27'$W (Bernhard et al., 2008). The observing site lies at an elevation of approximately 3200 meters above sea level and is surrounded by a snow-covered surface year-round. The instrument conducts scans of the solar spectral irradiance reaching the ground on a continuous basis during the sunlit period of the year. The measured quantity is the total, direct plus diffuse, solar irradiance striking the horizontal detector as a function of wavelength with a resolution of 0.63 nm. The primary mission of the instrument is to record solar ultraviolet irradiance at wavelengths from 290 nm to 400 nm. However, the instrument also observes visible sunlight, to a maximum wavelength of 600 nm. This work considers the Version 2 dataset (Bernhard et al., 2004) and uses the spectrally-integrated irradiance from 400 nm to 600 nm. The observations span the period from August 15, 2004 to October 23, 2014 and consist of 151,710 irradiance measurements.

Figure 1 presents the entire 400-600 nm irradiance database expressed as a function of solar zenith angle θ, where the minimum value encountered at Summit is 49-50^{o}. The scatter in Figure 1 for any value of θ represents the influence of clouds which, aside from a changing solar elevation, provide the major source of variability. This work considers deviations in ground-level solar irradiance from that expected for clear-sky conditions based on the "irradiance ratio" R, defined by:

$$R = E_M/E_{CLR} \tag{1}$$

where E_M is a measured 400-600 nm irradiance as in Figure 1, and E_{CLR} is the irradiance that would have existed at the time of the measurement, including absorption by ozone, had the sky been clear. The calculation of E_{CLR} assumes that the extraterrestrial solar irradiance is constant in time except for the variation associated with the changing Earth-sun distance over a year. Values of E_{CLR}, paired with each measured E_M, are part of the archived database. The ratio in Eq. 1 removes much of the dependence on solar zenith angle that is apparent in Figure 1, but transmission through clouds still causes R to vary with θ. This arises from the increasing slant path taken by direct sunlight though a cloud layer as θ grows, as well as from an increasing ratio of diffuse to direct irradiance incident on the top of a cloud.

Subsequent analyses use values of R sorted into specific ranges of θ where each range has a width of 0.1 in cos θ, and the data extend from cos θ = 0.0-0.1 to 0.6-0.7. To illustrate the data Figure 2 presents a histogram assembled from all irradiance ratios for the range cos θ = 0.2-0.3. The behavior shown here is typical of that in the remaining ranges. A major maximum exists for conditions close to a clear-sky, R=0.95-1.00. Somewhat thicker clouds corresponding to R = 0.675-0.775 lead to a secondary maximum, while skies with R<0.6 are infrequent. Figure 2 demonstrates that irradiance ratios in excess of the clear-sky value occur in 11-12% of the observations, with most of these being less than 1.05. These cases arise when the solar disk lies in the clear portion of a partly-cloudy sky as viewed from the sensor (Frederick and Erlick, 1997; Frederick and Hodge, 2011). In this circumstance, the direct solar irradiance is the same as in cloud-free conditions, while the diffuse component is enhanced over the value for clear skies. In addition, the high albedo of the surface at Summit contributes to enhancements in R when clouds are present.

Table 1 summarizes the statistical properties of the entire dataset by listing the number of data points in each range of cos θ, the number of calendar days spanned by the measurements, the mean irradiance ratio and the interquartile range, where 25% of the data lie below the stated lower limit and 25% lie above the upper limit. The seasonal cycle in solar elevation at high latitudes leads to a decreasing number of measurements as cos θ increases. When cos θ reaches 0.6-0.7, measurements exist for only a small number of days on either side of summer solstice, with no data at all in 2004 when measurements began in August. Owing to the limited dataset for cos θ = 0.6-0.7, this range is omitted from later statistical analyses.

Figure 3 presents the median irradiance ratio computed for each range of θ with the corresponding interquartile range. In general, the irradiance ratio decreases with increasing solar zenith angle, as expected for a direct solar beam passing through a plane parallel scattering layer. Note, however, that median irradiance ratio when the sun is very close to the horizon, cos θ = 0.0-0.1, is larger than when cos θ = 0.1-0.2. This is a consequence of a changing ratio of diffuse-to-direct solar irradiance. At the largest solar zenith angles, the diffuse component of irradiance incident on cloud tops is a larger percentage of the total irradiance than at smaller θ-values. The transmission of this diffuse irradiance through the cloud layer is greater than that of the direct component when θ is very large. The result is an uptick in mean irradiance ratio when the sun approaches the horizon. The behavior depicted in Table 1 and Figure 3 is qualitatively consistent with a model that treats a cloud as a horizontally-homogeneous scattering layer. However, a rigorous quantitative treatment is needed to replicate the details.

The following radiative transfer simulations utilize a model that evolved from that developed by Frederick and Lubin (1988) with later modifications to include clouds and a simple angular dependence in the diffuse radiance (Frederick and Hodge, 2011). The current version covers the visible wavelength band 400-600 nm and treats scattering by clouds via the delta-Eddington Approximation using an analytic phase function with asymmetry factor g=0.8 (Joseph et al., 1976). The modeled cloud layer covers the entire sky and has a specified optical thickness for scattering. The cloud is characterized by its albedo a_c for incident diffuse radiation to which the scattering optical thickness is directly related. The calculations adopt a high ground albedo, 0.97, appropriate to the surface at Summit (Carmagnola et al., 2013), and consider four cloud albedos, a_c=0.05, 0.10, 0.20 and 0.40.

Figure 4 presents mean irradiance ratios based on the measurements together with values computed from the radiative transfer model for the solar zenith angles θ_{MN} in Table 1. The curve for a_c=0.10 generally tracks the mean measured R-value. A comparison with Figure 3 indicates that cloud albedos encountered over Summit vary from less than 0.05 for the largest quartile of irradiance ratios to greater than 0.40 for the smallest quartile. The computed irradiance ratios are the sums of direct and diffuse components whose relative magnitudes vary with solar zenith angle. Figure 5 illustrates the direct and diffuse contributions for the cases a_c=0.10 and 0.20. As θ increases, the contribution of direct radiation transmitted through the optically-thin clouds decreases while the diffuse component increases. When $\theta<60^o$ and a_c=0.10, the direct contribution is larger than the diffuse, while enhanced scattering for a_c=0.20 leads to a diffuse irradiance in excess of the direct at all solar elevations encountered at Summit. Still, the decrease in direct irradiance with increasing θ determines the overall decline in R-values until θ exceeds 81-82^o. At still greater values of θ, the increasing fractional contribution of diffuse radiation leads to an increase in R as the sun nears the horizon.

For later work, the mean R-value based on all measurements in a given 24-hour period was computed to produce a dataset consisting of one irradiance ratio per day in each range of cos θ. This quantity is R(i) for given cos θ, where i=1,2,…N labels the day, and the number of days N on which data exist appears in Table 1. A seasonal cycle in the influence of cloudiness exists in the daily-mean data, although the day-to-day variability tends to obscure it. A moving average applied to the daily irradiance ratios reveals the greatest attenuation during the period from 2 to 11 weeks after the summer solstice. This seasonal dependence is of interest for climatic reasons since it modulates the total solar energy incident on the Greenland ice sheet during summer. In addition, the analysis of possible short-term responses to magnetic activity must account for this seasonal variation.

The procedure used to characterize the seasonal cycle in a specific range of cos θ combines data from all years to derive a shape as a function of time. This shape function is then scaled to fit data from each observing season separately, where the number of days measured from the June summer solstice, d_{ss}, of each year is a useful index of time. Data acquired during each observing season from 2004 through 2014 are centered on d_{ss}=0 and extend on both sides of the solstice, where the number of observing days depends on solar zenith angle. For example, the observing season for cos θ = 0.0-0.1 extends from d_{ss}= -141 to +142 days during each year, while that for cos θ = 0.2-0.3 extends from d_{ss}= -108 to +108 days. The shape of the seasonal cycle is determined by computing the average daily irradiance ratio for each value of d_{ss} using all years with data on this day number. In most cases, the average includes 10 or 11 values. These multi-year averages still contain considerable day-to-day variability as a function of d_{ss}. An 11-day running mean centered on each d_{ss} produces a smoother shape for the seasonal cycle. When d_{ss} lies less than 5 days from the beginning or ending date of an observing season, whatever data exist within a ±5 day window centered on d_{ss} enter the running average. This procedure provides the shape of a general seasonal cycle where data from all observing seasons influence the result. To determine the seasonal cycle for a particular observing season, this shape is scaled by a constant chosen to provide the best fit to each year individually.

Figure 6 presents the daily mean irradiance ratios during the observing season of 2014 for cos θ =0.2-0.3 with the corresponding seasonal cycle function for that year. The horizontal scale is d_{ss} in days, where d_{ss}=0 corresponds to the summer solstice. The seasonal cycle is apparent; the mean irradiance ratio over the period d_{ss}= -90 to -70 days is 0.92, while that for d_{ss}= 30 to 50 days is 0.79. This natural cycle is large relative to any short-term atmospheric response to magnetic activity, and it must be included in later statistical analyses.

3. Correlations between the Irradiance Ratio and Magnetic Activity at Various Time Lags

The next issue involves possible links between magnetic activity and the daily-mean irradiance ratio. The proxies of magnetic activity considered here are, first, the planetary A_p index and, second, the daily-averaged ground-level neutron flux, F_N, measured at Thule, Greenland. The A_p index is a widely-recognized measure of irregular, planetary-scale variability in the Earth's magnetic field over the course of one day (Perrone and DeFranceschi, 1998). Magnetic variations measured at ground-level at multiple stations, from which A_p is derived, arise from a changing flux of solar wind particles interacting with the magnetosphere. The neutron flux is correlated with A_p, since the geomagnetic field modulates incoming energetic cosmic rays whose degradation in the atmosphere produces the neutron showers. In general, an increase in the magnetic field is accompanied by a reduction in neutron flux (e.g. Lockwood, 1971).

The initial step is to examine correlations between R and A_p or between R and F_N. If these satisfy criteria identified below, then a more detailed investigation is warranted. Specifically, one must distinguish between correlations that clearly arise by chance and those that might point to an underlying physical connection. If a causal link exists between magnetic activity and atmospheric opacity, the processes at work will occur over a characteristic time scale and produce a time lag between the stimulus indicated by A_p (or F_N) and the response R. A change in atmospheric opacity in the visible part of the spectrum could arise from a change in the abundance of an absorber, an altered formation rate of condensation nuclei or a change in the rate of ice crystal growth. A reasonable time scale for such processes ranges from hours to, at most, several days. The measures of magnetic activity and atmospheric opacity used in this work are 24-hour averages. With this time resolution, an unusually large correlation of R with A_p (or F_N) where the date of the magnetic index precedes that of R by up to several days is compatible with, but cannot prove, a physical connection. A correlation where the time of A_p (or F_N) precedes that of R by more than several days, or where the magnetic index refers to a later date than R, is inconsistent with a physical link.

Based on the above reasoning, the first task is to determine if any unusually large correlations exist between magnetic activity and the irradiance ratio at time lags that are compatible with a mechanistic link. The following analysis adopts A_p as the index of magnetic activity, although analogous calculations could use the daily neutron flux F_N. Consider the simple regression:

$$R(i) = \beta_0 + \beta_1 A_p(\ell,i) + \varepsilon_R(i) \qquad [2]$$

for i=1,2,…,N. In Eq. 2 R(i) is the daily-mean irradiance ratio for day i of the multi-year data record in a specific range of cos θ, $A_p(\ell,i)$ is the magnetic index at lag ℓ days relative to R(i), $\varepsilon_R(i)$ is the residual, and β_0 and β_1 are ℓ-dependent coefficients to be estimated by least squares methods. A lag $\ell<0$ indicates that the value of A_p comes earlier in time than the measurement of R, and a result $\beta_1 \neq 0$ defines the correlation between the irradiance ratio and magnetic activity at the lag of ℓ days.

The calculations consider 1000 time lags in A_p from ℓ=-800 to +199 days, and the estimated coefficients $\beta_1(\ell)$ form a statistical distribution for each range of cos θ. Figures 7 and 8 are histograms of the resulting β_1-values for cos θ = 0.0-0.1 and 0.2-0.3, respectively. The great majority of these β_1-values are incompatible with a causal link between A_p and R either because the time lag between the two quantities is unacceptably long or, when $\ell>0$, unphysical. Instead, Figures 7 and 8 define the distributions of β_1-values that arise by chance. A physical connection cannot be ruled out only if two conditions are met. First, the associated lag ℓ must be a small negative number of days, and second, the associated β_1-value must deviate significantly from the distribution that arises by chance. This study adopts lags from ℓ=-7 to ℓ=0 days as defining the time frame during which a physical connection between A_p and R cannot be ruled out. If the β_1-value derived for one of these physically-interesting time lags also lies in the extreme of the histogram, then a more detailed investigation of the link between A_p and R for this particular lag is called-for.

Figures 9 and 10 present the coefficient β_1 versus ℓ over the range ℓ=-7 to ℓ =0 days for the bins cos θ = 0.0-0.1 and 0.2-0.3 respectively. Both curves have a maximum at lag ℓ=-1 day, as do analogous results for all other ranges of cos θ up to 0.6. The horizontal lines in Figures 9 and 10 are derived from results for all 1000 lags and define the largest 2.5% and 0.5% of the β_1-values. Finally, the vertical arrows on the abscissas in Figures 7 and 8 label the values of β_1 for ℓ = -1 day and confirm that they indeed lie in the positive extreme of the distributions.

Table 2 presents the value of β_1 derived for the lag ℓ = -1 day in each range of cos θ together with its rank relative to the 1000 lags considered, where a rank of 1 indicates the largest value. Also tabulated is the parameter t_{1000} which defines the distance of a specific β_1-value, measured in standard deviations, from the mean of the histogram defined by 1000 β_1-values. A quantitative interpretation of t_{1000} depends on the fact that each histogram is well-approximated by a normal distribution. In this case, the largest 25 values would meet the standard condition for statistical significance, $t_{1000} > 1.96$, while the largest 5 values would satisfy $t_{1000} > 2.58$. Table 2 shows that results for cos θ =0.0-0.1 and 0.3-0.4 exceed t_{1000} =1.96, while those for cos θ = 0.1-0.2 and 0.2-0.3 satisfy $t_{1000} > 2.58$. Furthermore, the β_1-value for cos θ = 0.2-0.3 is the largest of the 1000 coefficients, while those for cos θ = 0.0-0.1, 0.1-0.2 and 0.3-0.4 lie in the top 1.0-1.5%. Results for the bins cos θ = 0.4-0.5 and 0.5-0.6 fail to meet the standard of significance, although the β_1-values for a lag of -1 day still lie in the top 8.5% of all values.

Based on the criteria adopted here, the link between R and A_p at a lag of ℓ = -1 day merits additional study.

The ground-level neutron flux is an indicator of energetic particle inputs to high-latitudes, and one can readily envision a physical connection between ionization in the upper troposphere and atmospheric opacity (e.g. Kirkby et al., 2011). This prompted investigation into possible links between the daily-mean neutron flux measured at Thule and the irradiance ratio. Figure 11 presents the β_1-values derived via the regression:

$$R(i) = \beta_0 + \beta_1 F_N(\ell, i) + \varepsilon_R(i) \quad [3]$$

for the range ℓ = -7 to 0 days for all ranges satisfying $\cos\theta \leq 0.6$. No behavior that would suggest a connection between F_N and R appears at any of these physically-reasonable lags, and analysis of 1000 lags from ℓ = -800 to +199 days confirms that no result in the interval ℓ = -7 to 0 days is an outlier. Table 3 is analogous to Table 2 except the neutron flux at lag ℓ = -1 day replaces A_p. The negative β_1-values for $\cos\theta$ = 0.0-0.1, 0.1-0.2 and 0.2-0.3 fall in the smallest quartile of the 1000 cases, but while this is suggestive of a link, it is insufficient reject the hypothesis that no connection exists. The statistical link between R and A_p for lag ℓ=-1 day is clearly stronger than that between R and F_N. Despite the intuitive appeal of a coupling between atmospheric opacity and changes in the energetic particle flux on timescales of days, the data from Summit do not support a convincing statistical link between the two, and this work does not consider the neutron flux further.

4. Links between Atmospheric Opacity and A_p at a Time Lag of -1 Day

4.1. Analysis of Aggregated Data

The next task is to explore links between magnetic activity and atmospheric opacity at the time lag ℓ = -1 day in more detail, where this effort must account for the seasonal cycle in cloudiness. If periods of enhanced magnetic disturbance occurred, by chance, during times of year when cloudiness was minimal, then positive correlations between A_p and R would result. These correlations would be real in the mathematical sense, but would have no bearing on a potential causal connection. Next, a credible assessment of error bars is essential. The variance in A_p alone explains less than 1% of the variance in R, whose day-to-day changes are dominated by varying background cloudiness. This produces a large uncertainty range on estimated links between the two quantities.

The following investigations use two different measures of atmospheric opacity. The first is the irradiance ratio R, which contains the seasonal cycle and possibly trends. The second is the residual, ε_R, defined by the regression:

$$R(i) = g_0 + g_1 S(i) + g_2 T(i) + \varepsilon_R(i) \qquad [4]$$

where all quantities and regression coefficients, g_0, g_1, and g_2 refer to a specific range of cos θ, S(i) is the seasonal cycle term computed previously, T(i) provides for a linear trend in time, and i=1,2,…,N labels a daily-mean value. Any effect of magnetic variations that are uncorrelated with the seasonal cycle and trend is implicit in the residual ε_R. Application of Eq. 4 to the irradiance ratios produced a set of $\varepsilon_R(i)$, i=1,2,…N for each range of cos θ, where every $\varepsilon_R(i)$ is paired with one value of $A_p(i)$ at a lag of -1 day. The estimated values of g_2 were essentially zero in all cases, and the trend term has no influence on the conclusions.

To seek a dependence on magnetic activity, the datasets of R(i) and $\varepsilon_R(i)$ for each range of cos θ were split into five subsets based on the associated values of $A_p(i)$. These subsets are defined by $A_p<3$, $3\le A_p\le 5$, $5<A_p\le 10$, $10<A_p\le 16$ and $A_p>16$. Figure 12 presents the mean values of R for each subset of A_p in the cos θ ranges 0.0-0.1, 0.1-0.2, 0.2-0.3 and 0.3-0.4 plotted versus the mean value of A_p for each grouping. To facilitate easy comparison, all R-values were scaled so that the value for $A_p<3$ equals 1.0 in each range of cos θ. Figure 13 presents analogous results for the mean values of ε_R where no normalization is needed. No definitive pattern appears in Figures 12 and 13 when $A_p \leq 16$, but when $A_p>16$ both R and ε_R show obvious increases. The mean residual based on irradiance ratios with $A_p>16$ exceeds that for data with $A_p \leq 16$ by $1.0\text{-}1.1 \times 10^{-2}$ or 1.2-1.3% of the mean R-value for cos θ = 0.0-0.4. Note that results based on the residuals are free of any bias associated with the seasonal cycle.

It is essential to assess the statistical significance of the behavior in Figures 12 and 13. The daily-mean irradiance ratios for a specific range of cos θ can be divided into two subsets, one linked to relatively small values of A_p and the other to relatively large values. A statistical t-test is able to determine if irradiance ratios in the large-A_p bin differ significantly from those in the small-A_p bin. Although this is a standard test (e.g. Rice, 1968), it is useful to summarize the concepts as they apply in this work. Consider two samples consisting of N_1 and N_2 points selected from the database of irradiance ratios in a range of cos θ. The mean irradiance ratios computed for these samples are R_1 and R_2, respectively. If these are random samples drawn from the same population, their means will differ due only to sampling errors. If one compares many such pairs, the collection of differences R_2-R_1 will form a distribution with a mean of 0.0 and standard deviation σ_{12} given by:

$$\sigma_{12} = (N_1^{-1} + N_2^{-1})^{1/2}\sigma \qquad [5]$$

where σ is the standard deviation of the entire population. However, if the difference R_2-R_1 for a specific pair of samples is anomalously large, one can reject the hypothesis that R_1 and R_2 represent the same population with a high level of confidence. This circumstance would arise if the irradiance ratio varies with A_p. In this context, the magnitude of any one difference R_2-R_1 is judged relative to the standard deviation σ_{12}. If the parameter t defined as an absolute value:

$$t = \left|(R_2-R_1)/\sigma_{12}\right| \quad [6]$$

exceeds 1.96, the probability that the two samples are random samples of the same population is less than 5%. When t reaches 2.58, the probability is less than 1%, where these numerical values apply when N_1+N_2 is greater than about 150 (Panofsky and Brier, 1968). This quantitative interpretation requires that the set of differences R_2-R_1 form a normal distribution, and the accuracy of this assumption must be tested as part of the analysis. An identical line of reasoning applies when the deseasonalized residuals ε_R replace irradiance ratios in the t-test.

The issue is to determine if samples of irradiance ratios or deseasonalized residuals defined by their associated values of A_p have the characteristics expected of random samples drawn from the same population. The test proceeds by splitting the irradiance ratios and residuals into subsets, the small-A_p bin defined by $A_p(i) \leq A_p^*$ and the large-A_p bin with $A_p(i) > A_p^*$. Three trials adopted different values for the boundary A_p^*; these are A_p^*=16, A_p^*=25 and A_p^*=32 where the value of A_p^* fixes the sample sizes N_1 and N_2.

As noted above, interpretation of the t-statistic in terms of 95% or 99% confidence limits requires the differences in means based on numerous random samples, to follow normal distributions. If the original data are normally distributed, this is satisfied, but Figure 2 shows that the irradiance ratios fail to satisfy this condition. To confirm the usefulness of the t-statistic, a series of simulations examined the properties of the differences. Each simulation selected N_1 values of R(i) and ε_R(i) at random and computed their means, R_1 and ε_1, where the value selected for A_p^* fixes N_1. The remaining N_2=N-N_1 values of R(i) and ε_R(i) form the means R_2 and ε_2. These values, together with the standard deviations based on all N values, allow the calculation of t as described above. This procedure was repeated 1000 times using different random selections of N_1 and N_2 points. The results show that normal distributions provide good approximations to the histograms assembled from the 1000 R_2-R_1 and ε_2-ε_1 values in each range of cos θ. As an example, Figure 14 presents the histogram of the residuals ε_2-ε_1 for cos θ = 0.2-0.3 and A_p^*=25. The standard deviation derived by fitting a normal distribution to Figure 14 is within 1.3% of that deduced from Eq. 5. Similar results apply to the other ranges of cos θ.

The simulations provide a significance test in addition to the t-statistic. One can rank order the 1000 simulated differences, from largest to smallest, and the position of the difference based on A_p^* in this ranking is a measure of significance. Table 4 presents results for the irradiance ratio differences R_2-R_1, and Table 5 gives analogous results using the residuals, ε_2-ε_1. For each range of cos θ and each value of A_p^*, the tables include the t-statistic based on Eqs. 5 and 6 and the number of simulated differences, out of 1000, that exceed the true difference, either R_2-R_1 or ε_2-ε_1, based on A_p^*. One requires t>1.96 or a ranking of 25 or smaller to claim, with a confidence level of 95% or higher, that the sample with $A_p>A_p^*$ represents a different population than that for $A_p \leq A_p^*$.

By the standards outlined above, Table 4 shows a significant dependence of the irradiance ratio on the magnetic index for all values of A_p^* and all ranges of cos θ up through 0.4. Table 5, which adjusts for the seasonal cycle in cloudiness, also shows statistically significant results for cos θ≤0.4 when A_p^*=32, but as the value of A_p^* shrinks, significant results shift to progressively smaller values of cos θ. When A_p^*=16, only the difference for cos θ = 0.0-0.1 exceeds the 95% confidence criterion, although for cos θ in the three ranges from 0.1-0.4 only 27 to 58 of the 1000 simulated differences exceed the true values. The values in Tables 4 and 5 show a significant positive link between magnetic activity and atmospheric opacity at Summit.

However, differences between results based on the irradiance ratios and the residuals imply that some, but not all, of the correlation arises from an uneven distribution of magnetic disturbances over the seasonal cycle.

4.2. Analysis based on Linear Regression

The analysis in Section 4.1 aggregated data into bins that encompass a broad range of A_p-values. This approach allows only a coarse resolution when estimating the variation of ground-level irradiance with magnetic activity, and it does not provide an evaluation of uncertainties. In contrast, regression models that relate R to the A_p index at a lag of -1 day utilize the full continuum of magnetic indices and produce rigorous error bars, but the results assume a linear relationship. A useful model is:

$$R(i) = g_0 + g_1 S(i) + g_2 T(i) + g_3 A_p(i) + \varepsilon(i) \qquad [7]$$

where the coefficients g_0, g_1, g_2 and g_3 are estimated separately for each range of cos θ, and S(i) and T(i) are as defined in Eq. 4. Initial applications of Eq. 7 produced a residual ε(i) with autocorrelation at a time lag of one day, indicating that the irradiance ratio on day i is not independent of conditions on day i-1. An upgraded model includes this by imposing the condition:

$$\varepsilon(i) = \varepsilon_0(i) + \kappa\varepsilon(i-1) \qquad [8]$$

where the value of κ is to be estimated. The added coefficient creates a nonlinearity in Eq. 7 and requires an iterative solution for κ and the remaining coefficients. Derived values of κ vary from 0.08 to 0.12 for different ranges of cos θ, and tests show that ε_0 is free of autocorrelation at a lag of -1 day. Finally, the estimates of g_0, g_1 and g_2 differed insignificantly from 0.0, 1.0 and 0.0 respectively.

Values of g_3 estimated from Eqs. 7 and 8 quantify the link between atmospheric opacity and magnetic activity, but an assessment of the uncertainty range on g_3 is critical to the conclusions. The calculation of confidence limits on g_3 uses the residuals ε_0 to generate 1000 datasets of simulated irradiance ratios. The statistical distribution of residuals for each simulated dataset is identical to that of ε_0, but the specific residual assigned to any given simulated irradiance ratio is selected at random. Regressions based on Eq. 7 using the 1000 simulated datasets then generate a statistical distribution of g_3-values whose width defines 95% and 99% confidence limits on the best-estimate of g_3. The Appendix presents details of the calculation.

A statistically significant correlation between atmospheric opacity and A_p requires that the 95% confidence range on g_3 not encompass 0.0. Table 6 presents the best estimate of g_3 for each range of cos θ as well as the 95% and 99% confidence limits. These values differ from 0.0 with a confidence level of 95% or higher for all values of $\cos\theta \leq 0.4$, while estimates for $\cos\theta = 0.0$-0.1 and 0.2-0.3 reach the 99% level of confidence. A convenient way to express results is to state the percent change in irradiance ratio δ for a change in the magnetic index of $\Delta A_p = +20$ units. This is close to the difference in mean A_p values between the bin with $A_p>16$ in Figure 13 and the bins with $A_p \leq 16$. The expression is:

$$\delta = 100\, g_3\, \Delta A_p / R_{MN} \qquad [10]$$

where R_{MN} is the mean irradiance ratio for the range of cos θ considered. Table 7 presents δ and its 95% confidence limits for the ranges with $\cos\theta \leq 0.4$, the solar elevations where significant links between R and A_p exist. In view of the similarity in results for different ranges of cos θ, it is reasonable to summarize them by the single average in the last row in Table 7. In a mean sense, two days which differ by +20 units in the one-day lagged magnetic index differ by +1.10% in their irradiance ratios, where the 95% confidence range is 0.20-2.00%.

The regression model of Eq. 7 assumes a linear dependence of R on A_p, while Figures 12 and 13 show no clear relationship for $A_p \leq 16$ and a sharp increase in R for $A_p > 16$. The mean value of A_p for all data with $A_p \leq 16$ is $A_p = 6.6$, while the mean for all data with $A_p > 16$ is $A_p = 28.7$. Use of the average value of δ from Table 7 implies an irradiance ratio for $A_p = 28.7$ which exceeds that for $A_p = 6.6$ by 1.22±0.99%, in excellent agreement with the percentage difference derived directly from Figure 13. Although the relationship between R and A_p appears to be nonlinear, the single value $\delta = 1.10 \pm 0.90\%$ per +20 unit change in A_p provides a convenient estimate of differences in R between magnetically quiet and disturbed periods.

5. Discussion and Conclusions

The statistical distribution of 400-600 nm irradiance ratios observed at Summit shows two maxima, one near 0.70-0.75, corresponding to relatively thin clouds, and the other at 0.95-1.0, for nearly-clear conditions. As the solar zenith angle increases from 51^o to 82^o, the long-term mean irradiance ratio decreases from about 0.97-0.98 to 0.82-0.83. This attenuation is consistent with radiative transfer calculations based on a highly reflective lower boundary and cloud layers whose mean albedo for diffuse radiation is near 0.1, with the middle 50% of the measurements encompassing albedos from less than 0.05 to greater than 0.4.

The high latitude of Summit makes it an interesting location at which to seek possible atmospheric responses to magnetic activity. It is essential to account for the seasonal cycle in cloud-attenuation since periods of magnetic disturbance are distributed unevenly over the year and thereby lead to the possibility of mathematically-real, but physically-uninteresting, correlations with atmospheric opacity. After allowance for the seasonal cycle, a positive correlation exists between the irradiance ratio in specific ranges of solar zenith angle and the magnetic A_p index on the previous day. This link appears in aggregated data sorted according to the A_p-value and in regression models that assume a linear relationship between the irradiance ratio and A_p.

A mechanistic interpretation of the results must address the magnitude and sign of the link between R and A_p as well as the dependence on solar elevation, where significant couplings appear only at solar zenith angles that satisfy $\cos\theta \leq 0.4$. This dependence on $\cos\theta$ rules out short-term changes in the extraterrestrial solar irradiance, related to A_p, as a cause of the coupling. Any such changes would appear in the numerator of Eq. 1 at all values of $\cos\theta$, and not just at $\cos\theta \leq 0.4$. The fact that significant correlations between R an A_p appear only when the sun is relatively low in the sky suggests that the mechanism lies in the transmission properties of the atmosphere. Atmospheric processes responsible for the correlations might operate at any altitude from thermosphere to troposphere and could involve changes in absorption or scattering. Regarding changes in absorption, a decrease in atmospheric ozone or nitrogen dioxide amounts would lead to a percentage enhancement in the 400-600 nm irradiance which increases with solar zenith angle.

The clear-sky irradiances E_{CLR} used to produce the irradiance ratios via Eq. 1 include ozone amounts appropriate to each measurement, so in principle the R-values are independent of ozone. However, an offset between the true ozone amount implicit in E_M in Eq. 1 and that used to compute E_{CLR} would lead to a dependence of R on column ozone. Ultraviolet irradiances measured by the Summit spectroradiometer allow a check to ensure that variations in ozone are not responsible for the results in Table 6. The ratio of irradiances measured in the wavelength bands 312.5-317.5 nm and 307.7-312.5 nm is an index of column ozone. Daily-mean values of this ratio showed no significant correlation to the R-values or to the A_p index. Based on this negative outcome, one can dismiss variations in column ozone as an intermediary that creates the statistical link between R and A_p.

Dissociation and ionization by energetic particles lead to production of nitric oxide in the high-latitude stratosphere (Nicolet, 1975). Subsequent reactions form nitrogen dioxide which absorbs solar radiation at wavelengths between 400 and 600 nm. If a short-term decrease in nitric oxide production took place in association with changes in A_p, this could be accompanied by a decrease in the NO_2 concentration. The absorption cross sections of Voigt et al. (2002) and the column densities observed by Noxon (1975) from a high-elevation site in Colorado allow an estimate of the attenuation provided by atmospheric NO_2. Based on these values, the complete elimination of atmospheric NO_2 would lead to an increase in the 400-600 nm irradiance ratio of about 3%, 0.6% and 0.3% for $\cos \theta = 0.05$, 0.25 and 0.45 respectively. The dependence of these percentages on $\cos \theta$ differs from that in Table 7, and the reduction required in NO_2 abundance to reproduce the sensitivity of R to A_p appears unacceptably large. Based on these estimates, it is unlikely that changes in NO_2 can be responsible for the coupling between R and A_p.

An alternate mechanism that might lead to the deduced statistical links involves changes in atmospheric scattering after periods of magnetic disturbance. A horizontally homogeneous scattering layer acts to decrease the direct component of solar irradiance and increase the diffuse component received at the ground, where the net effect depends on the layer's albedo, the degree of bias toward forward scattering and the ground albedo. The following radiative transfer simulations examine the sensitivity of the irradiance ratio to changes in atmospheric scattering at tropospheric altitudes. The model atmosphere contains a horizontally-homogeneous cloud layer whose albedo for diffuse irradiance is a_c. The asymmetry factor for scattering in the cloud is g=0.8, and the resulting irradiance ratio is R. A change in albedo Δa_c, due to the growth or shrinkage of a scattering layer, leads to a change ΔR in the irradiance ratio, where the quantity:

$$P = (\Delta R/\Delta a_c)/R \qquad [11]$$

is the fractional sensitivity of the irradiance ratio to changes in albedo, including both the direct and diffuse contributions.

Figure 15 presents the sensitivities as functions of solar zenith angle where curves appear for skies with background cloudiness described by a_c = 0.05, 0.10 and 0.15. The greatest negative sensitivity appears at $\theta=81.6^o$ for skies with optically thin clouds, a_c = 0.05 and 0.10, and at $\theta=75.5^o$ when a_c=0.15. For smaller solar zenith angles, $\theta\leq65^o$, the sensitivity weakens. In general, the sensitivity to changes in scattering is greatest when the effect of background cloudiness is minimal and the solar zenith angle exceeds 70^o. The dependence of P on solar zenith angle is broadly compatible with that deduced from the Summit data. Furthermore, the atmospheric changes required to produce increases in irradiance ratio of the type associated with magnetic activity are reasonable. A small decrease in albedo, $\Delta a_c \sim -10^{-3}$ to -10^{-2}, will produce an increase in irradiance ratio of the proper magnitude.

Since the deduced change in R following a magnetically-disturbed day is positive, the above scenario requires a negative correlation between the albedo of an existing scattering layer and A_p. This result is model-dependent and arises from the assumption of a horizontally-homogeneous scattering layer that covers the entire sky, including the solar disk. An increase in the albedo of an optically thin layer that did not obscure the solar disk as observed from a ground-based sensor would be accompanied by an enhanced irradiance ratio. The possible scenarios are numerous and involve changes in fractional sky-coverage, the altitude of the altered scattering, the albedos of the scattering layers and the asymmetry factor. A change in atmospheric scattering appears to be the most likely explanation for the correlation between R and A_p. However, given the unconstrained variables, one cannot state whether the response to magnetic activity consists of a decrease in the albedos of existing scattering layers that block the sun or an increase in thin scattering layers that do not, in general, cover the solar disk.

The linear regressions imply that a +20 unit difference in A_p between two days is accompanied by a difference in irradiance ratio of about 1.10% of the long-term mean value, where the associated 95% confidence range is 0.20-2.00%. This estimate is consistent with deductions from data aggregated into bins of A_p, where mean R-values for A_p>16 exceed those for $A_p \leq 16$ by 1.2-1.3%. These results suggest, but cannot prove, a causal relationship between magnetic activity and atmospheric opacity over Summit. A confirmation of the results identified here using independent data from other high-latitude sites would be of value. Although slight changes in atmospheric scattering following periods of enhanced magnetic activity offer a plausible explanation for the results, a quantitative understanding of solar-terrestrial couplings that might explain the relationships is not yet available.

Appendix A: Derivation of 95% and 99% Confidence Ranges on the Regression Coefficient g_3

The following procedure allows estimating confidence limits on the regression coefficient g_3 that quantifies the link between the irradiance ratio and A_p at a time lag of -1 day. First, the best-estimate regression coefficients g_0, g_1, g_2, g_3 and the residuals $\varepsilon_0(i)$, i=1,2,…N, are determined by applying Eqs. 7 and 8 in the text to the actual irradiance ratios. These residuals are the basis for defining uncertainty limits on g_3. The approach treats the $\varepsilon_0(i)$ as random errors to generate 1000 datasets of simulated irradiance ratios, $R_S(i,j)$, i=1,2,…,N and j=1,2,…,1000 via expression:

$$R_S(i,j) = g_0 + g_1S(i) + g_2T(i) + g_3A_p(i) + \kappa\varepsilon_S(i-1,j) + \varepsilon_{0S}(i,j) \quad [A.1]$$

The coefficients g_0, g_1, g_2, g_3 and κ are the best-estimates derived from Eqs . 7 and 8, $\varepsilon_S(i\text{-}1,j)$ is known from the previous time step, and $\varepsilon_{0S}(i,j)$ is selected at random from the residuals of the original regression using Eq. 7, specifically, $\varepsilon_{0S}(i,j) = \varepsilon_0(i_R)$ where i_R is a randomly-chosen integer between 1 and N for each i and j. The 1000 simulated sets of irradiance ratios have the same dependence on A_p as the actual dataset, and the residuals $\varepsilon_s(i,j)$ for fixed j form the same statistical distribution as the actual residuals, $\varepsilon_0(i)$. But the random assignment of the residuals, leads to values of $R_S(i,j)$ which differ from the actual dataset, R(i), and therefore to different estimates of the regression coefficients for each value of j.

Application of the original regression model in Eqs. 7 and 8 to the simulated datasets produces 1000 estimates of the regression coefficients whose statistical distributions define uncertainty limits on the original coefficients g_0, g_1, g_2, g_3 and κ. The spread among the 1000 values of each coefficient arises from the variance that remains unexplained by Eq. 7, which is typically near 85% of the total. These unaccounted-for variations arise primarily from day-to-day changes in cloudiness over the observing site, and except for the small autocorrelation, they are seemingly random.

Figures A.1 and A.2 are histograms constructed from the 1000 g_3-values derived for $\cos\theta$ = 0.0-0.1 and 0.2-0.3, respectively. These distributions, and those for the remaining ranges of $\cos\theta$, allow assigning uncertainty limits to g_3. The 95% confidence range is defined as extending from a lower limit $g_L(95)$ to an upper limit $g_U(95)$. Similarly, the 99% confidence range extends from $g_L(99)$ to $g_U(99)$. The lower end of the 95% confidence range is fixed by requiring that 25 of the 1000 simulated g_3-values be smaller than $g_L(95)$, and the upper end satisfies the condition that 25 values exceed $g_U(95)$. Derivation of the 99% confidence range is analogous, where the 10 smallest and 10 largest g_3-values define the limits. This procedure requires no assumptions about the mathematical form of the histograms; although Figures A.1 and A.2 closely resemble normal distributions, there can be deviations in the wings. As a consequence, the best-estimate of g_3 may not fall exactly in the center of the 95% and 99% confidence limits.

Acknowledgements: The operation of the spectroradiometer at Summit and the data processing was supported by the National Science Foundation, Office of Polar Programs under agreement ARC-1203250 with Biospherical Instruments, Inc. The Bartol Research Institute neutron monitor program was supported by the National Science Foundation under grants ANT-0739620 and ANT-0838839, and by the University of Delaware Department of Physics and Astronomy. The author thanks Germar Bernhard for valuable discussions during the course of this work.

References

Almeida, J., et al., 2013. Molecular understanding of sulphuric acid-amine particle nucleation in the atmosphere. Nature 502, 359-363, doi:10.1038/nature12663.

Bernhard, G., Booth, C.R., Ehramjian, J.C., 2004. Version 2 data of the National Science Foundation's Ultraviolet Radiation Monitoring Network: South Pole. J. Geophys. Res. 109, D21207, doi:10.1029/2004JD004937.

Bernhard, G., Booth, C.R., and Ehramjian, J.C., 2008. Comparison of UV irradiance measurements at Summit, Greenland; Barrow, Alaska; and South Pole, Antarctica. Atmos. Chem. Phys. 8, 4799-4810.

Carmagnola, C. M., Domine, F., Dumont, M., Wright, P., Strellis, B., Bergin, M., Morin, S., 2013. Snow spectral albedo at Summit, Greenland: measurements and numerical simulations based on physical and chemical properties of the snowpack. The Cryosphere, 7(4), 1139-1160.

Dickinson, R.E., 1975. Solar variability and the lower atmosphere. Bull. Am. Meteorol. Soc. 56, 1240-1248.

Frederick, J.E., Lubin, D., 1988. The budget of biologically active ultraviolet radiation in the Earth-atmosphere system. J. Geophys. Res. 93, 3825-3832.

Frederick, J.E., Erlick, C., 1997. The attenuation of sunlight by high latitude clouds: Spectral dependence and its physical mechanisms. J. Atmos. Sci. 54, 2813-2819.

Frederick, J. E., Hodge, A. L., 2011. Solar irradiance at the earth's surface: long-term behavior observed at the South Pole. Atmos. Chem. Phys. 11, 1177-1189, doi:10.5194/acp-11-1177-2011.

IPCC, 2013: Summary for Policymakers. In: Climate Change 2013: The Physical Science Basis.

Contribution of Working Group I to the Fifth Assessment Report of the Intergovernmental Panel on Climate Change [Stocker, T.F., Qin, D., Plattner, G.-K., Tignor, M., Allen, S.K., Boschung, J., Nauels, A., Xia, Y., Bex, V., Midgley, P.M. (eds.)]. Cambridge, UK.

Joseph, J.H., Wiscombe, W.J., Weinman, J.A., 1976. The delta-Eddington approximation for radiative flux transfer. J. Atmos. Sci. 33, 2452–2459.

Kazil, J., Lovejoy, E.R., Barth, M.C., O'Brien, K., 2006. Aerosol nucleation over oceans and the role of galactic cosmic rays. Atmos. Chem. Phys. 6, 4905-4924, doi:10.5194/acp-6-4905-2006.

Kirkby, J., et al., 2011. Roles of sulphuric acid, ammonia and galactic cosmic rays in atmospheric aerosol nucleation. Nature 476, 429-433, doi:10.138/nature10343.

Laken, B.A., Kniveton, D.R., 2011. Forbush decreases and Antarctic cloud anomalies in the upper troposphere. J. Atmos. Sol. Terr. Phys. 73, 371-376, doi:10.1016/j.jastp.2010.03.008.

Laken, B.A., Palle, E., Calogovic, J., Dunne, E.M., 2012. A cosmic ray-climate link and cloud observations. J. Space Weather Space Clim. 2, A18, doi:10.1051/swsc/2012018.

Lockwood, J. A., 1971. Forbush decreases in cosmic ray intensity. Space Science Rev. 12, 688-715.

Nicolet, M., 1975. On the production of nitric oxide by cosmic rays in the mesosphere and stratosphere. Planet. Space Sci. 23, 637-649.

Noxon, J.F., 1975. Nitrogen dioxide in the stratosphere and troposphere measured by ground-based absorption spectroscopy. Science 189, 547-549.

Panofsky, H.A., Brier, G.W., 1968. Some Applications of Statistics to Meteorology. The Pennsylvania State University, University Park, PA.

Perrone, L., De Franceschi, G., 1998. Solar, ionospheric and geomagnetic indices. Annali di

Geofisica 41, 843-855.

Rice, J.A., 1988. Mathematical Statistics and Data Analysis, Wadsworth and Brooks/Cole Statistics/Probability Series. Pacific Grove, CA, ISBN 0-534-08247-5.

Roberts, W.O., Olson, R.H., 1973. Geomagnetic storms and wintertime 300 mb trough development in the North Pacific-North America area. J. Atmos. Sci. 30, 135-140.

Roldugin, V.C., Tinsley, B.A., 2004. Atmospheric transparency changes associated with solar wind-induced atmospheric electricity variations. J. Atmos. Sol. Terr. Phys. 66, 1143-1149, doi:10.1016/j/jastp.2004.05.006.

Sloan, T., Wolfendale, A.W., 2013. Cosmic rays, solar activity and the climate. Environ, Res. Lett. 8, doi:10.1088/1748-9326/8/4/045022

Svensmark, H., Friis-Christensen, H.E., 1997. Variation of cosmic ray flux and global cloud coverage – a missing link in solar-climate relationships. J. Atmos. Sol. Terr. Phys. 59, 1225-1232.

Svensmark, H., Bondo, T., Svensmark, J., 2009. Cosmic ray decreases affect atmospheric aerosols and clouds. Geophys. Res. Lett. 36, L15101, doi:10.1029/2009GL038429.

Svensmark, H., Enghoff, M.B., Pedersen, J.O.P., 2013. Response of cloud condensation nuclei (> 50 nm) to changes in ion-nucleation. Phys. Lett. A 377, 2343-2347.

Tinsley, B.A., 2008. The global atmospheric electric circuit and its effects on cloud microphysics, Rep. Prog. Phys. 71, doi:10.1088/0034-4885/71/6/066801.

Tinsley, B.A., Brown, G.M., Scherrer, P.H., 1989. Solar variability influences on weather and climate: possible connections through cosmic ray fluxes and storm intensification. J. Geophys. Res. 94, 14783–14792.

Tinsley, B.A., Burns, G.B. and Zhou, L., 2007. The role of the global electric circuit in solar and internal forcing of clouds and climate. Adv. Space Res. 40, 1126-1139.

S. Voigt, S., J. Orphal, J. and Burrows, J.P., 2002. The temperature and pressure dependence of the absorption cross-sections of NO_2 in the 250-800 nm region measured by Fourier-transform spectroscopy. J. Photochem. Photobiol. A: Chemistry 149, 1–7.

Wilcox, J.M., Scherrer, P.H., Svalgaard L., Roberts, W.O., Olson R.H., 1973. Solar magnetic structure: relation to circulation of the Earth's atmosphere. Science. 180, 185-186.

Wilson, C.T.R., 1920. Investigations on lightning discharges and on the electric field and thunderstorms. Phil. Trans. Roy. Soc. London. A 221, 73–115.

Table 1. Summary of the Database from Summit in Each Range of Solar Zenith Angle

Range of cos θ	θ_{MN}*	Number of Measurements	Number of Days: N	Mean R	Interquartile Range
0.0-0.1	87.1	31,615	2,560	0.8547	0.7679-0.9410
0.1-0.2	81.6	29,614	2,354	0.8292	0.7031-0.9573
0.2-0.3	75.5	23,850	2,033	0.8609	0.7443-0.9726
0.3-0.4	69.6	21,871	1,722	0.8906	0.7968-0.9787
0.4-0.5	63.3	19,470	1,399	0.9225	0.8577-0.9851
0.5-0.6	56.7	17,081	1,027	0.9523	0.9139-0.9920
0.6-0.7	51.2	8,209	552	0.9767	0.9567-1.0029

*θ_{MN} is the mean value of the solar zenith angle based on all irradiance ratios that fall in the indicated range of cos θ.

Table 2. Results of Regression of Irradiance Ratio R on A_p with a Lag of -1 Day in A_p

Bin of cos θ	β_1	t_{1000}	Rank*
0.0-0.1	5.59×10^{-4}	2.55	13
0.1-0.2	7.86×10^{-4}	2.61	9
0.2-0.3	8.19×10^{-4}	2.72	1
0.3-0.4	7.24×10^{-4}	2.40	15
0.4-0.5	3.02×10^{-4}	1.20	85
0.5-0.6	2.27×10^{-4}	1.35	72

*A rank of 1 indicates that β_1 for a lag of -1 day between A_p and R was the largest value out of 1000 cases with lags ranging from -800 to +199 days.

Table 3. Results of Regression of Irradiance Ratio R on the Thule Neutron Flux (F_N) with a Lag of -1 Day in F_N

Bin of cos θ	β_1	t_{1000}	Rank*
0.0-0.1	-4.91×10^{-5}	-1.10	177
0.1-0.2	-4.22×10^{-5}	-0.99	208
0.2-0.3	-3.68×10^{-5}	-0.92	228
0.3-0.4	-2.75×10^{-5}	-0.07	422
0.4-0.5	-1.10×10^{-5}	+0.52	701
0.5-0.6	-1.16×10^{-5}	-0.12	468

*A rank of 1 indicates that β_1 for a lag of -1 day was the smallest value out of 1000 cases with lags between F_N and R ranging from -800 to +199 days.

Table 4. Statistical t-Test Applied to Irradiance Ratios in Each Bin of Solar Zenith Angle

cos θ	t (A_p^*=16)	Rank* (A_p^*=16)	t (A_p^*=25)	Rank* (A_p^*=25)	t (A_p^*=32)	Rank* (A_p^*=32)
0.0-0.1	3.17	1	2.47	7	2.70	2
0.1-0.2	2.80	2	3.36	1	3.74	0
0.2-0.3	2.70	2	3.20	0	3.36	0
0.3-0.4	2.93	5	2.81	1	2.51	5
0.4-0.5	1.53	59	1.87	28	1.94	21
0.5-0.6	1.83	30	0.95	171	1.32	88

*Rank refers to the number of cases out of 1000 pairs of random samples in which the difference R_2-R_1 exceeds the difference obtained when the samples are defined by the critical value A_p^*. The value of A_p^* determines the sample sizes used in the t-tests.

Table 5. Statistical t-Test Applied to Residuals in Each Bin of Solar Zenith Angle

cos θ	t (A_p^*=16)	Rank* (A_p^*=16)	t (A_p^*=25)	Rank* (A_p^*=25)	t (A_p^*=32)	Rank* (A_p^*=32)
0.0-0.1	2.60	6	2.01	24	2.53	3
0.1-0.2	1.71	39	2.16	19	3.12	1
0.2-0.3	1.60	58	2.05	17	2.74	3
0.3-0.4	1.95	27	1.88	35	2.29	12
0.4-0.5	0.83	207	1.23	101	1.71	41
0.5-0.6	1.10	142	0.58	288	1.18	113

*Rank refers to the number of cases out of 1000 pairs of random samples in which the difference ε_2-ε_1 exceeds the difference obtained when the samples are defined by the critical value A_p^*. The value of A_p^* determines the sample sizes used in the t-tests.

Table 6. Coefficients g_3 that Relate the Irradiance Ratio to A_p at a Time Lag of -1 Day derived via Linear Regression

cos θ	Estimated g_3*	95% Confidence Range in g_3	99% Confidence Range in g_3
0.0-0.1	4.14×10^{-4}	$(0.95 \text{ to } 7.37) \times 10^{-4}$	$(0.07 \text{ to } 8.25) \times 10^{-4}$
0.1-0.2	4.82×10^{-4}	$(0.53 \text{ to } 8.87) \times 10^{-4}$	$(-0.96 \text{ to } 9.86) \times 10^{-4}$
0.2-0.3	5.19×10^{-4}	$(1.24 \text{ to } 9.60) \times 10^{-4}$	$(0.30 \text{ to } 10.51) \times 10^{-4}$
0.3-0.4	4.71×10^{-4}	$(0.73 \text{ to } 8.46) \times 10^{-4}$	$(-0.47 \text{ to } 9.04) \times 10^{-4}$
0.4-0.5	2.03×10^{-4}	$(-1.25 \text{ to } 5.31) \times 10^{-4}$	$(-2.23 \text{ to } 6.47) \times 10^{-4}$
0.5-0.6	1.48×10^{-4}	$(-1.53 \text{ to } 4.30) \times 10^{-4}$	$(-2.23 \text{ to } 5.47) \times 10^{-4}$

*Estimated values of g_3 are based on Eqs. 7 and 8 and account for the seasonal cycle.

Table 7. Percent Change in Irradiance Ratio δ for a Change in Magnetic Index of +20 Units Estimated via Linear Regression

cos θ	δ (%) for ΔA_p=+20*	95% Confidence Range for δ (%)*
0.0-0.1	0.98	0.22 – 1.74
0.1-0.2	1.16	0.12 – 2.14
0.2-0.3	1.20	0.28 – 2.24
0.3-0.4	1.06	0.16 – 1.90
Mean	1.10	0.20 – 2.00

*Values based on regression using values of A_p at a time lag of -1 day. Percent changes are expressed relative to the mean irradiance ratio in each range of cos θ.

Figure Captions

Figure 1. Measured irradiances for the 400 nm to 600 nm wavelength band expressed as functions of solar zenith angle. The data cover the period August 15, 2004 to October 23, 2014.

Figure 2. Histogram of irradiance ratios R for the solar zenith angle range cos θ = 0.2-0.3.

Figure 3. Ratios of measured irradiance to clear-sky irradiance expressed as functions of solar zenith angle θ. Symbols refer to the median, upper limit of the smallest quartile and lower limit of the largest quartile for 7 ranges of θ defined by cos θ =0.0-0.1 to 0.6-0.7.

Figure 4. Computed irradiance ratios as functions of solar zenith angle for cloud layers with albedos for diffuse radiation of a_c=0.05, 0.10, 0.20 and 0.40. Also shown are means based on the observed daily values.

Figure 5. Contributions of direct and diffuse components to the total irradiance ratio computed for cloud layers with albedos for diffuse radiation of a_c=0.1 and a_c=0.2. The cloud albedo for each curve is given in parentheses.

Figure 6. Daily-mean irradiance ratios for cos θ = 0.2-0.3 during the observing season of 2014 (points) with the seasonal cycle function (open squares). The horizontal scale is day-number measured from June 21.

Figure 7. Histogram of the coefficient β_1 relating the A_p index and the irradiance ratio R for cos θ = 0.0-0.1. The distribution is based on 1000 values derived for time lags between A_p and R from ℓ = -800 to +199 days. The arrow on the abscissa identifies β_1=5.59x10^{-4} derived for ℓ = -1 day.

Figure 8. Histogram of the coefficient β_1 relating the A_p index and the irradiance ratio R for cos θ = 0.2-0.3. The distribution is based on 1000 values derived for time lags between A_p and R from ℓ = -800 to +199 days. The vertical line segment identifies β_1=8.19x10^{-4} derived for ℓ = -1 day.

Figure 9. Dependence of the coefficient β_1 on the time lag ℓ between the A_p index and irradiance ratio R for ℓ = -7 to 0 days. Results refer to cos θ = 0.0-0.1. Dashed horizontal lines indicate the largest 2.5% and 0.5% of values derived for all lags from ℓ = -800 to +199 days.

Figure 10. Dependence of the coefficient β_1 on the time lag ℓ between the A_p index and irradiance ratio R for ℓ = -7 to 0 days. Results refer to cos θ = 0.2-0.3. Dashed horizontal lines indicate the largest 2.5% and 0.5% of values derived for all lags from ℓ = -800 to +199 days.

Figure 11. Dependence of the coefficient β_1 on the time lag ℓ between the daily-mean neutron flux from Thule and the irradiance ratio R for ℓ = -7 to 0 days. Results appear for all ranges that satisfy cos $\theta \leq 0.6$.

Figure 12. Mean irradiance ratio versus mean value of the A_p index at a lag of -1 day. The five intervals of A_p are defined by $A_p<3$, $3\leq A_p\leq 5$, $5<A_p\leq 10$, $10<A_p\leq 16$ and $A_p>16$. Different symbols refer to the ranges cos θ = 0.0-0.1, 0.1-0.2, 0.2-0.3 and 0.3-0.4. Each irradiance ratio was normalized to 1.0 for the point with $A_p<3$.

Figure 13. Mean residual ε_R versus mean value of the A_p index at a lag of -1 day. The five intervals of A_p are defined by $A_p<3$, $3\leq A_p\leq 5$, $5<A_p\leq 10$, $10<A_p\leq 16$, and $A_p>16$. Different symbols refer to the ranges cos θ = 0.0-0.1, 0.1-0.2, 0.2-0.3 and 0.3-0.4.

Figure 14. Histogram of the differences between residuals, ε_2-ε_1, based on 1000 pairs of random samples drawn from the database for cos θ = 0.2-0.3. A normal distribution provides a good approximation to the differences.

Figure 15. Sensitivity of ground-level irradiance to changes in cloudiness expressed as a function of solar zenith angle. Curves apply to skies with background cloud albedos of 0.05, 0.15 and 0.25.

Figure A.1. Histogram constructed from 1000 g_3-values derived from simulated irradiance ratio datasets with cos θ = 0.0-0.1. The width of the histogram defines confidence limits on the estimate of g_3.

Figure A.2. Histogram constructed from 1000 g_3-values derived from simulated irradiance ratio datasets with $\cos\theta = 0.2\text{-}0.3$. The width of the histogram defines confidence limits on the estimate of g_3.

Figure 1

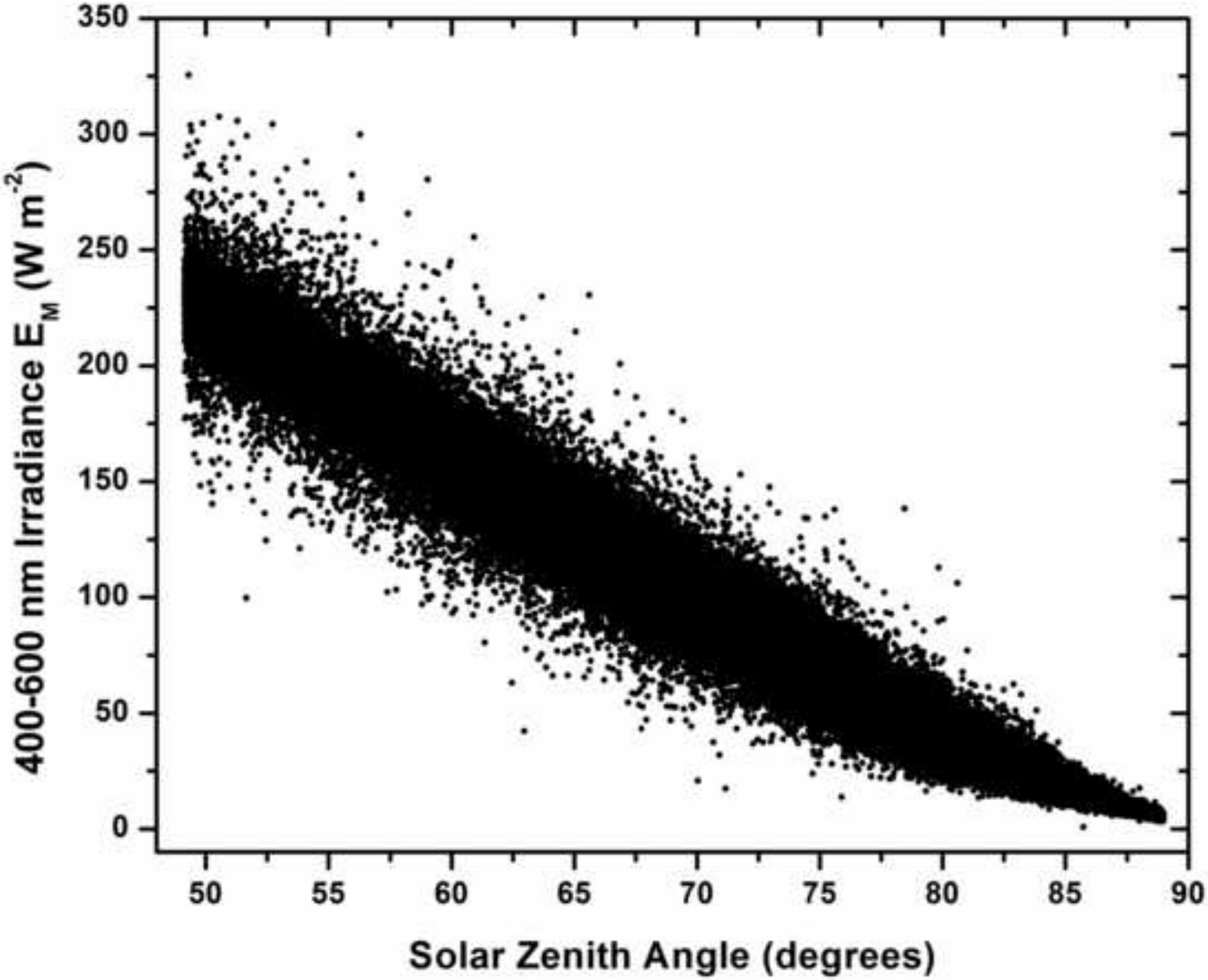

400-600 nm Irradiance E_M (W m^{-2})
350
300
250
200
150
100
50
0
50
55
60
65
70
75
80
85
90
Solar Zenith Angle (degrees)

Figure 2

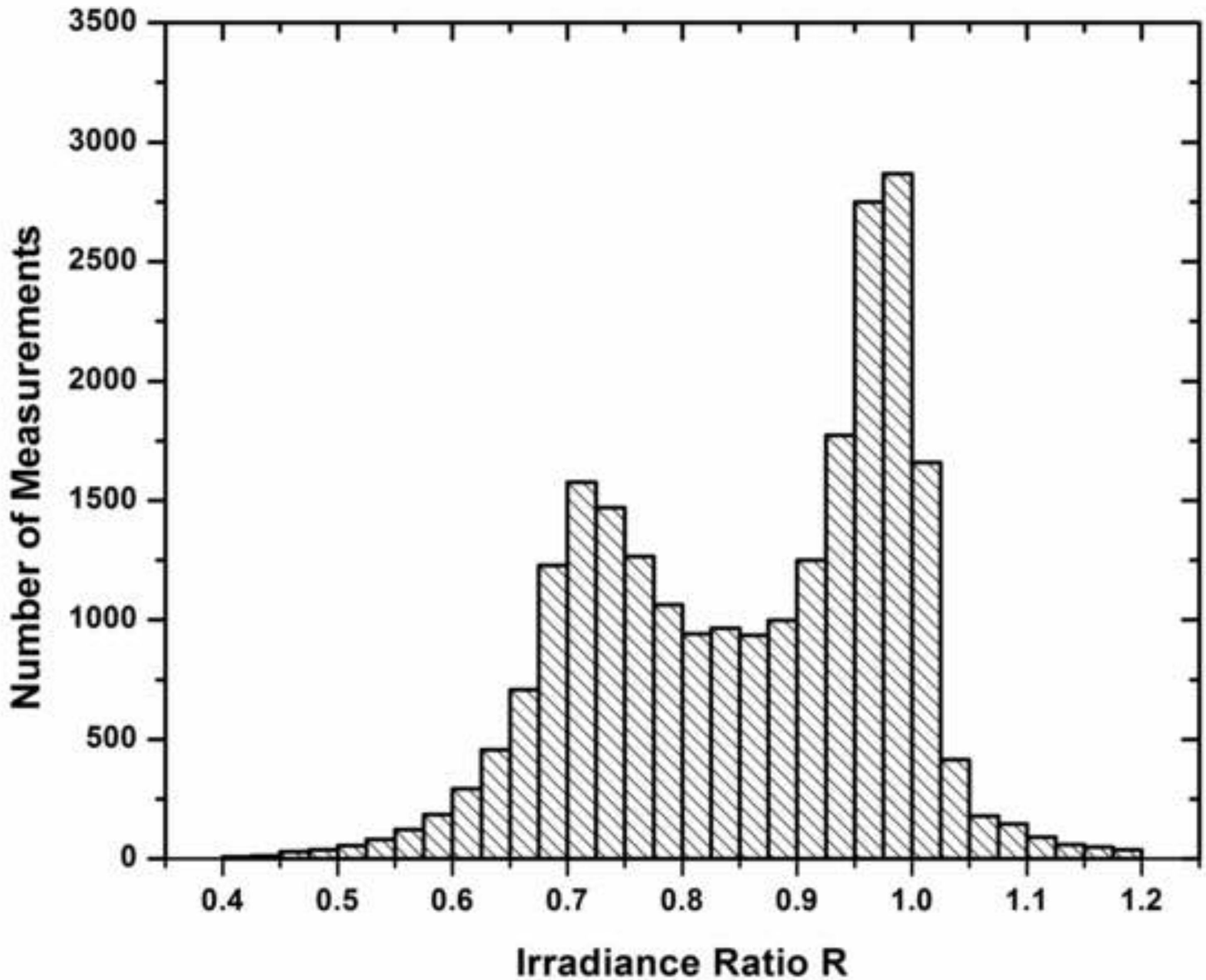
3500
3000
2500
2000
1500
1000
500
0
Number of Measurements
0.4
0.5
0.6
0.7
0.8
0.9
1.0
1.1
1.2
Irradiance Ratio R

Figure 3

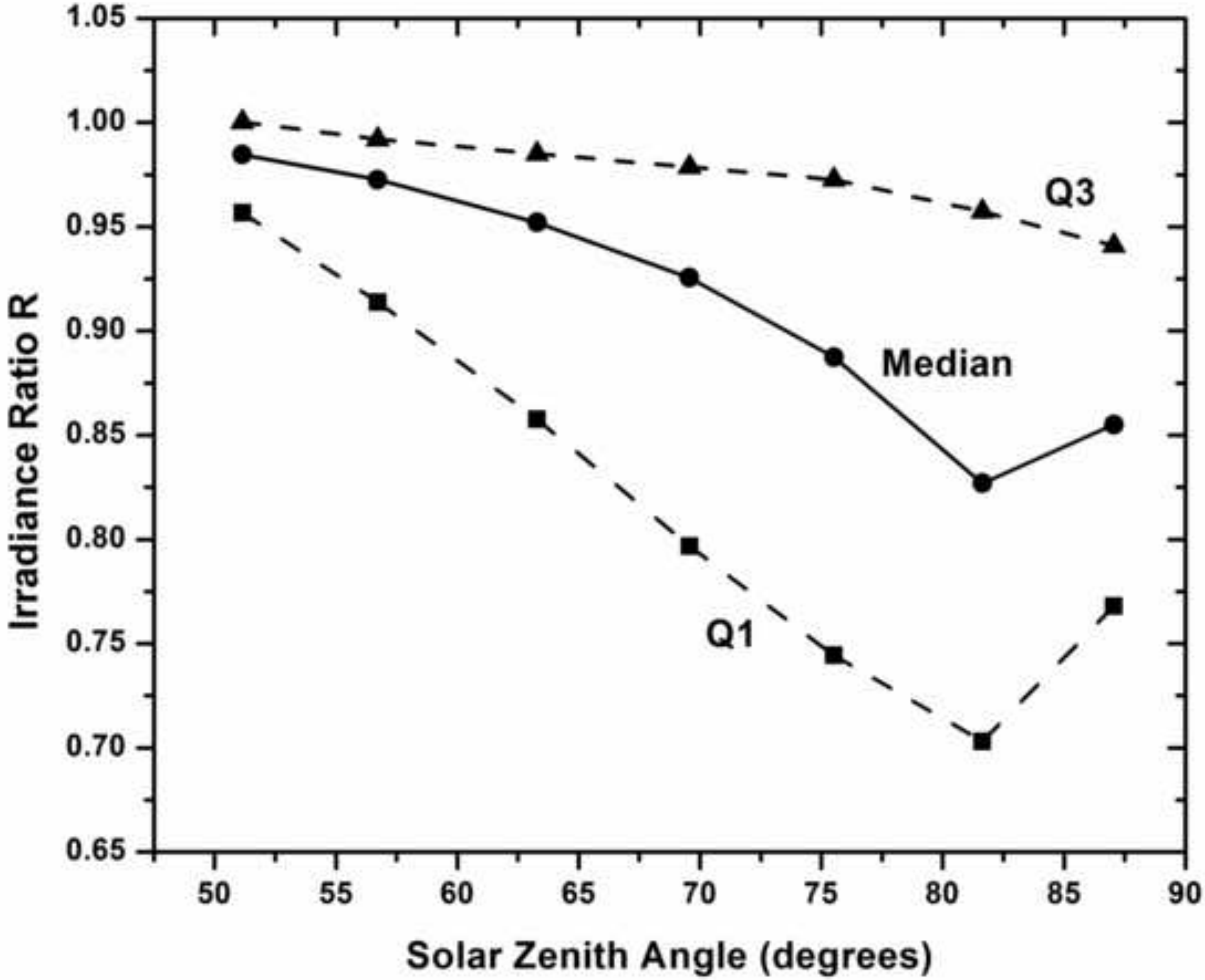

1.05
1.00
0.95
0.90
0.85
0.80
0.75
0.70
0.65
Irradiance Ratio R
50
55
60
65
70
75
80
85
90
Solar Zenith Angle (degrees)
Q3
Median
Q1

Figure 4

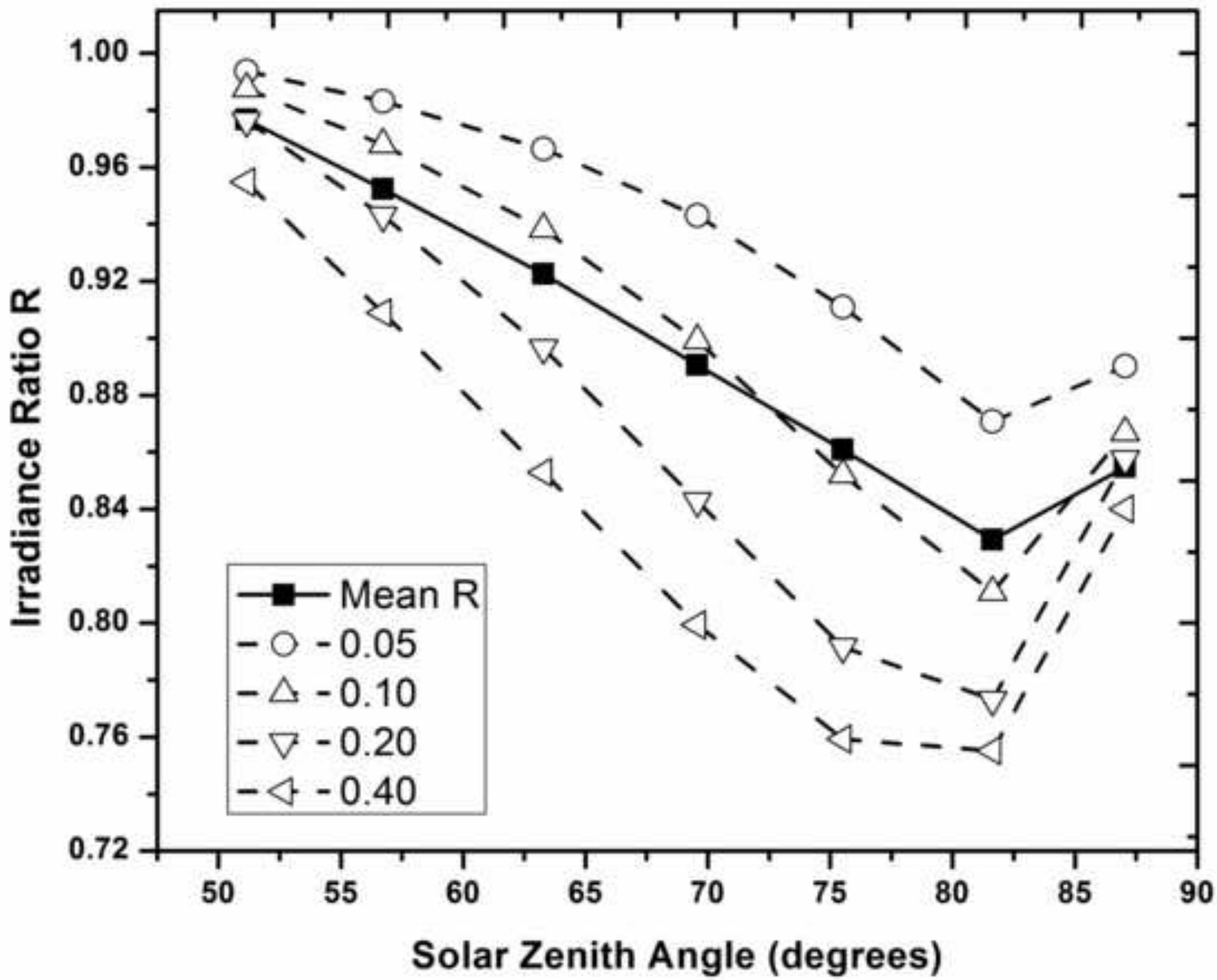

Irradiance Ratio R
1.00
0.96
0.92
0.88
0.84
0.80
0.76
0.72
50
55
60
65
70
75
80
85
90
Solar Zenith Angle (degrees)
Mean R
0.05
0.10
0.20
0.40

Figure 5

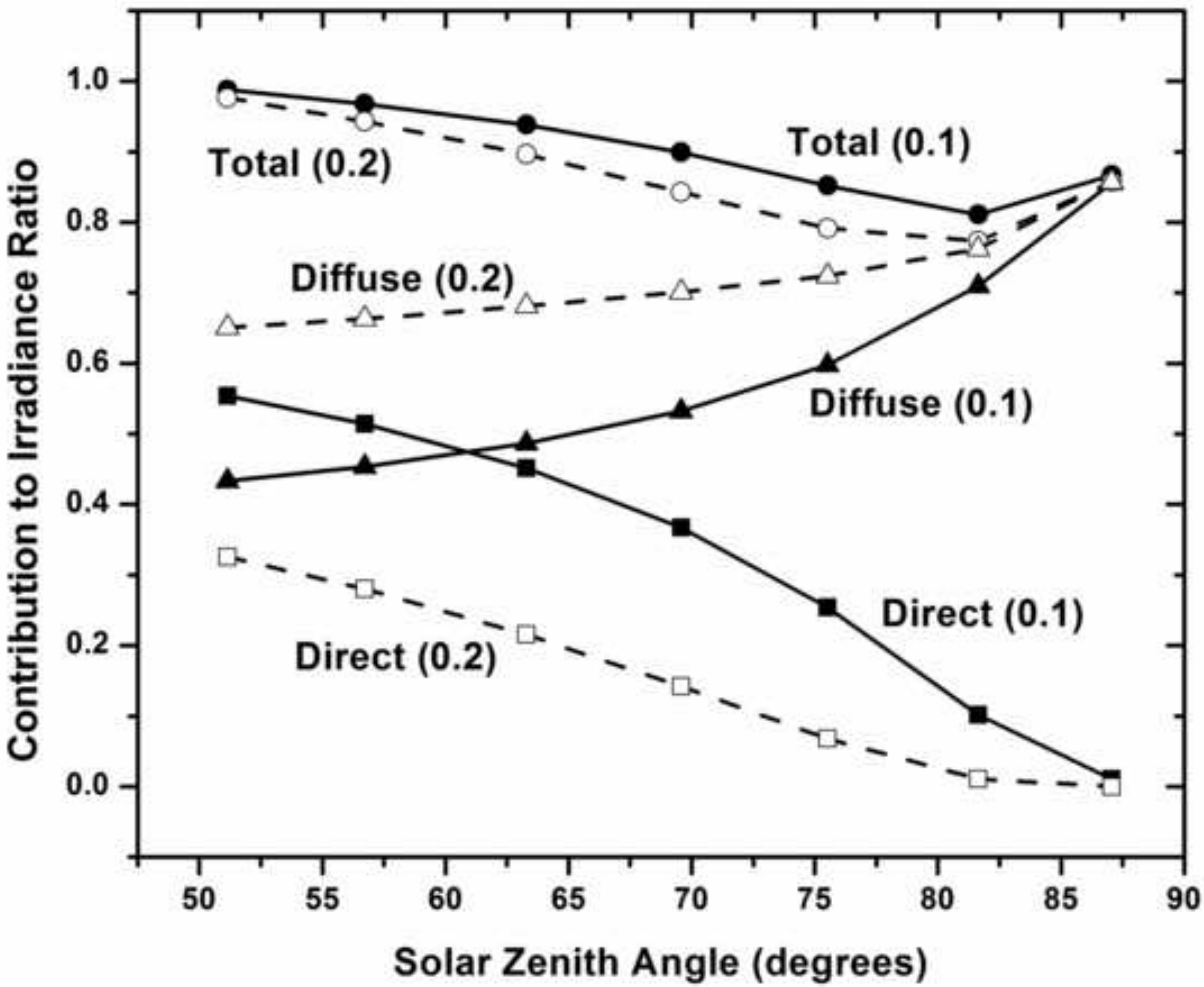

Total (0.1)
Total (0.2)
Diffuse (0.2)
Diffuse (0.1)
Direct (0.1)
Direct (0.2)
Contribution to Irradiance Ratio
Solar Zenith Angle (degrees)
1.0
0.8
0.6
0.4
0.2
0.0
50
55
60
65
70
75
80
85
90

Figure 6

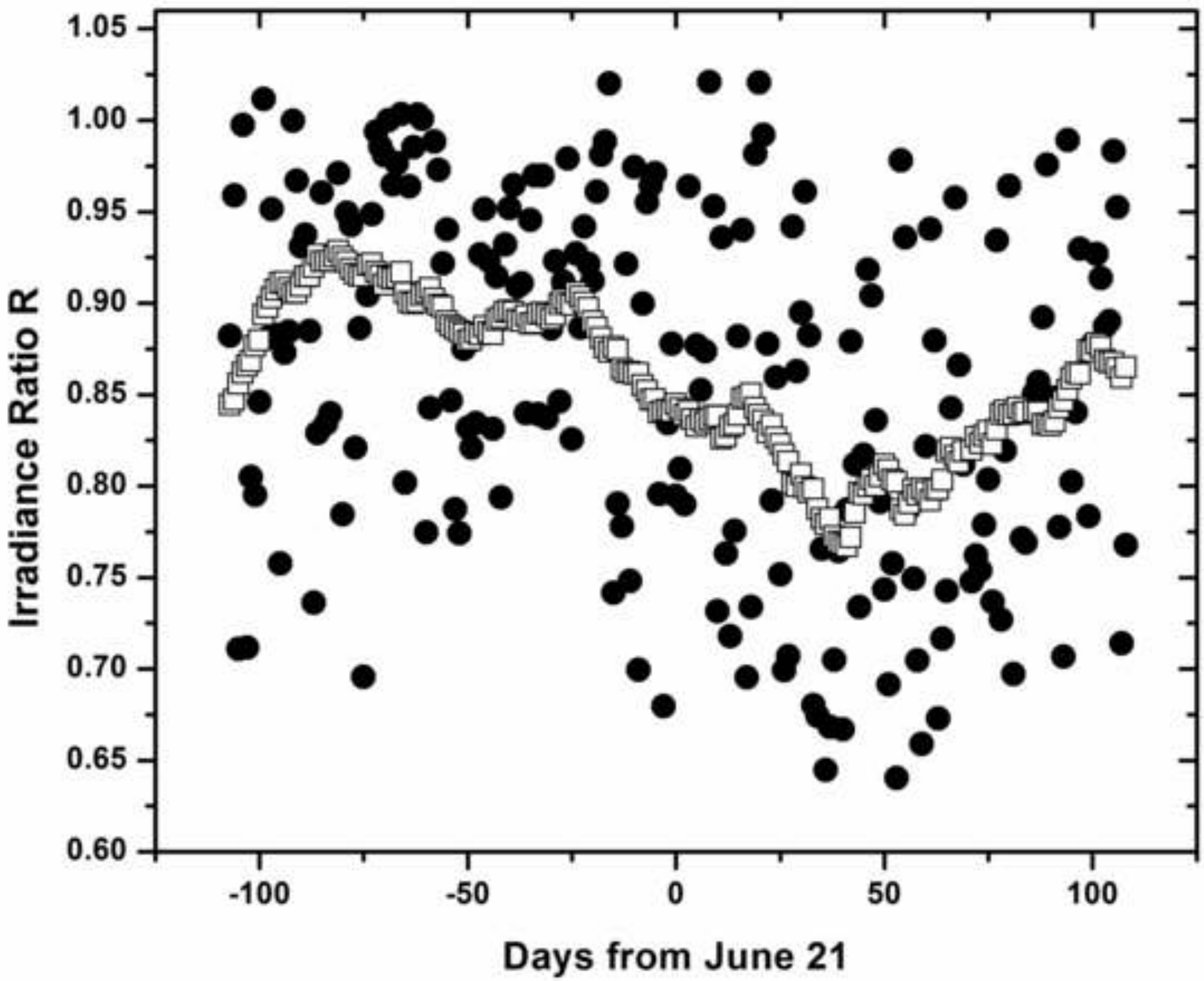

1.05
1.00
0.95
0.90
0.85
0.80
0.75
0.70
0.65
0.60
Irradiance Ratio R
-100
-50
0
50
100
Days from June 21

Figure 7

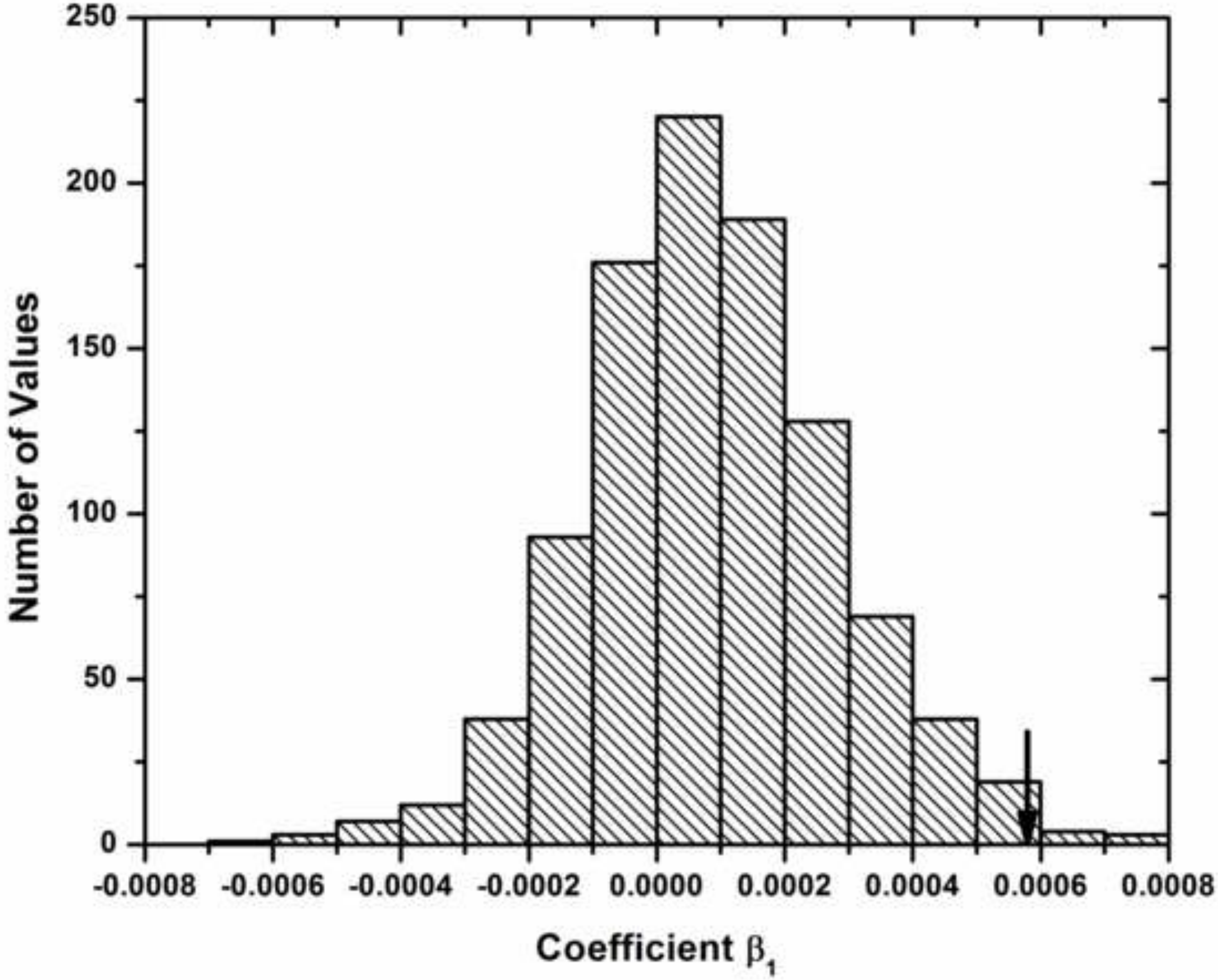

250
200
150
100
50
0
Number of Values
-0.0008
-0.0006
-0.0004
-0.0002
0.0000
0.0002
0.0004
0.0006
0.0008
Coefficient β_1

Figure 8

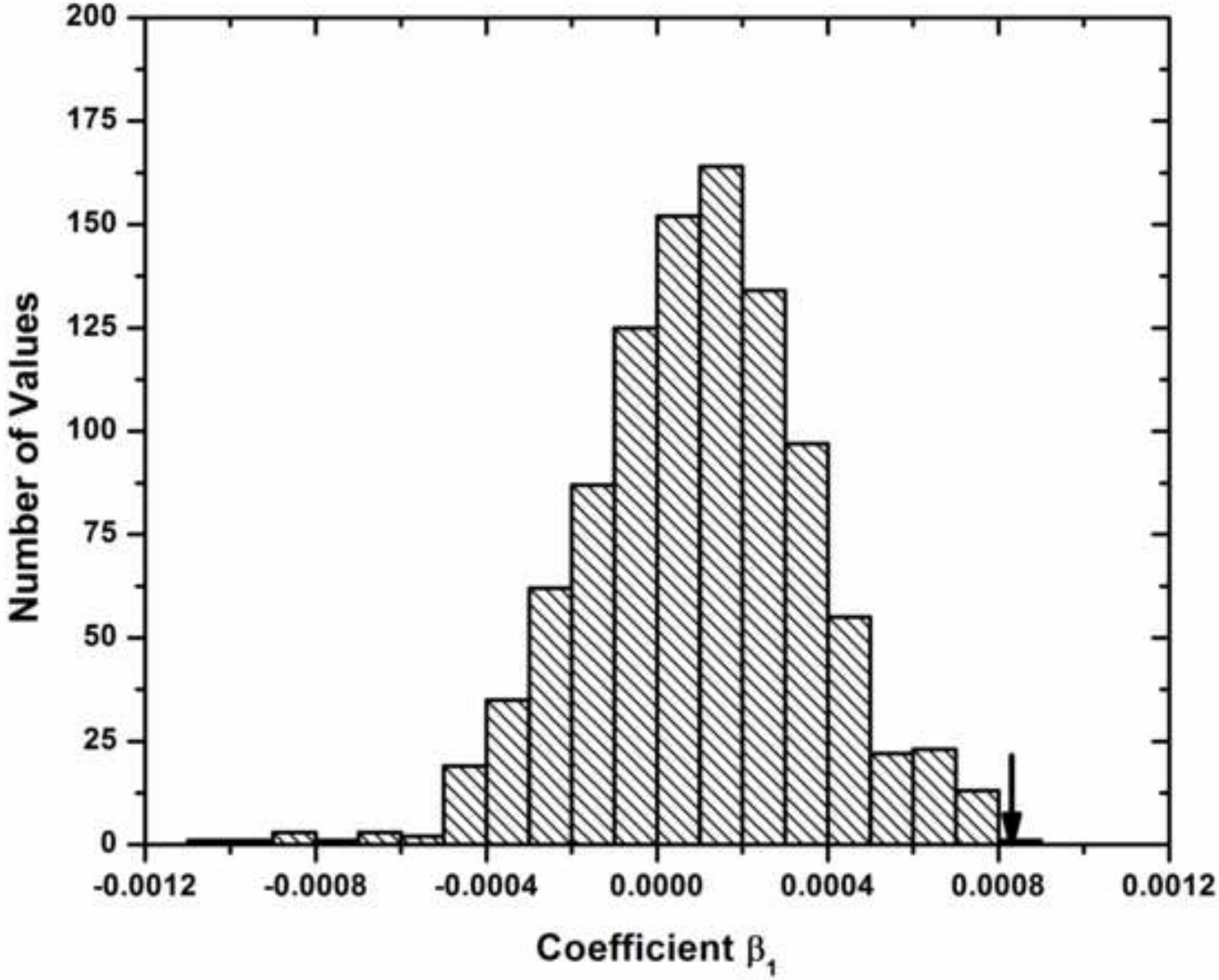

200
175
150
125
100
75
50
25
0
Number of Values
-0.0012
-0.0008
-0.0004
0.0000
0.0004
0.0008
0.0012
Coefficient β_1

Figure 9

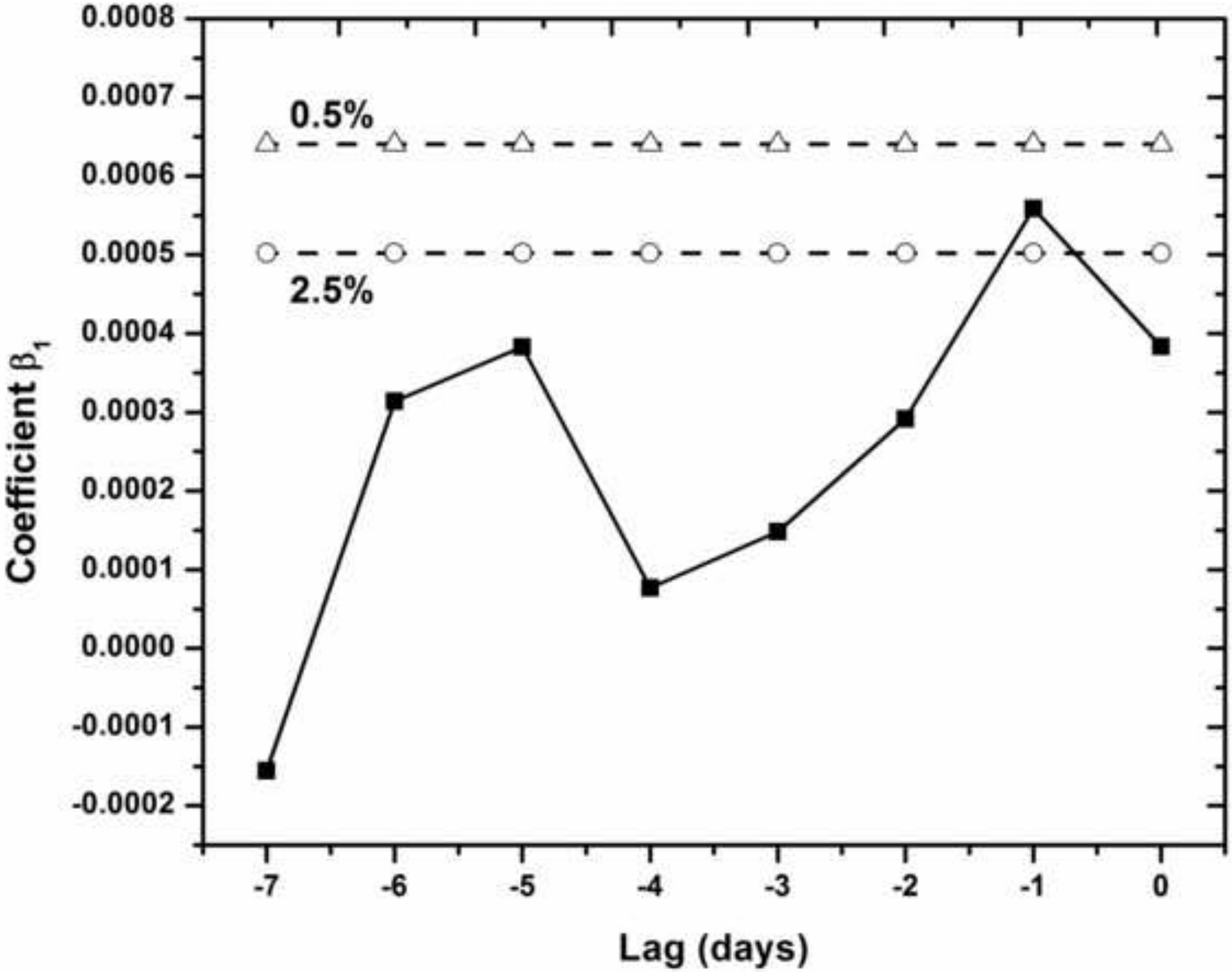

0.0008
0.0007
0.0006
0.0005
0.0004
0.0003
0.0002
0.0001
0.0000
-0.0001
-0.0002
0.5%
2.5%
Coefficient β_1
-7
-6
-5
-4
-3
-2
-1
0
Lag (days)

Figure 10

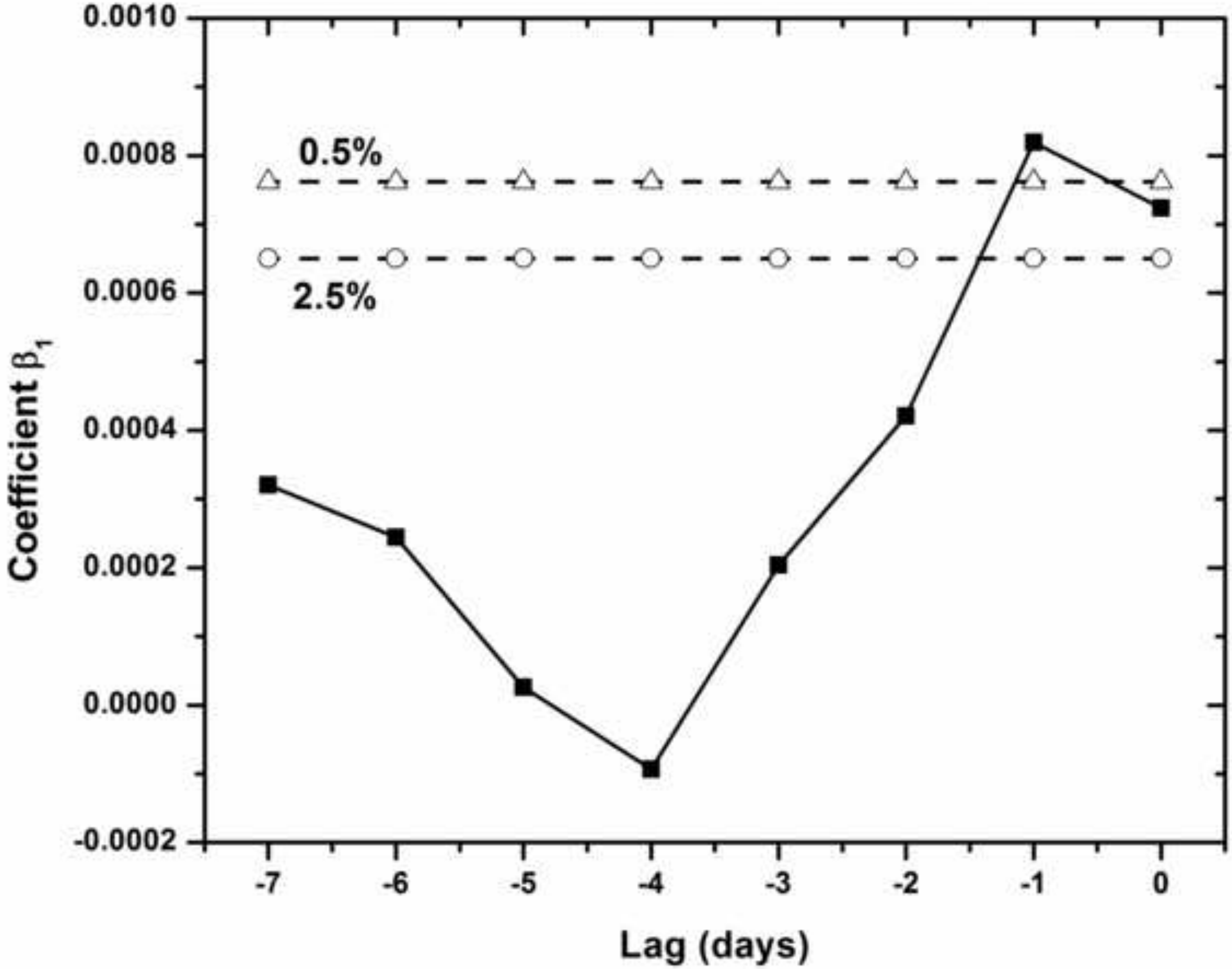

0.0010
0.0008
0.0006
0.0004
0.0002
0.0000
-0.0002
0.5%
2.5%
Coefficient β_1
-7
-6
-5
-4
-3
-2
-1
0
Lag (days)

Figure 11

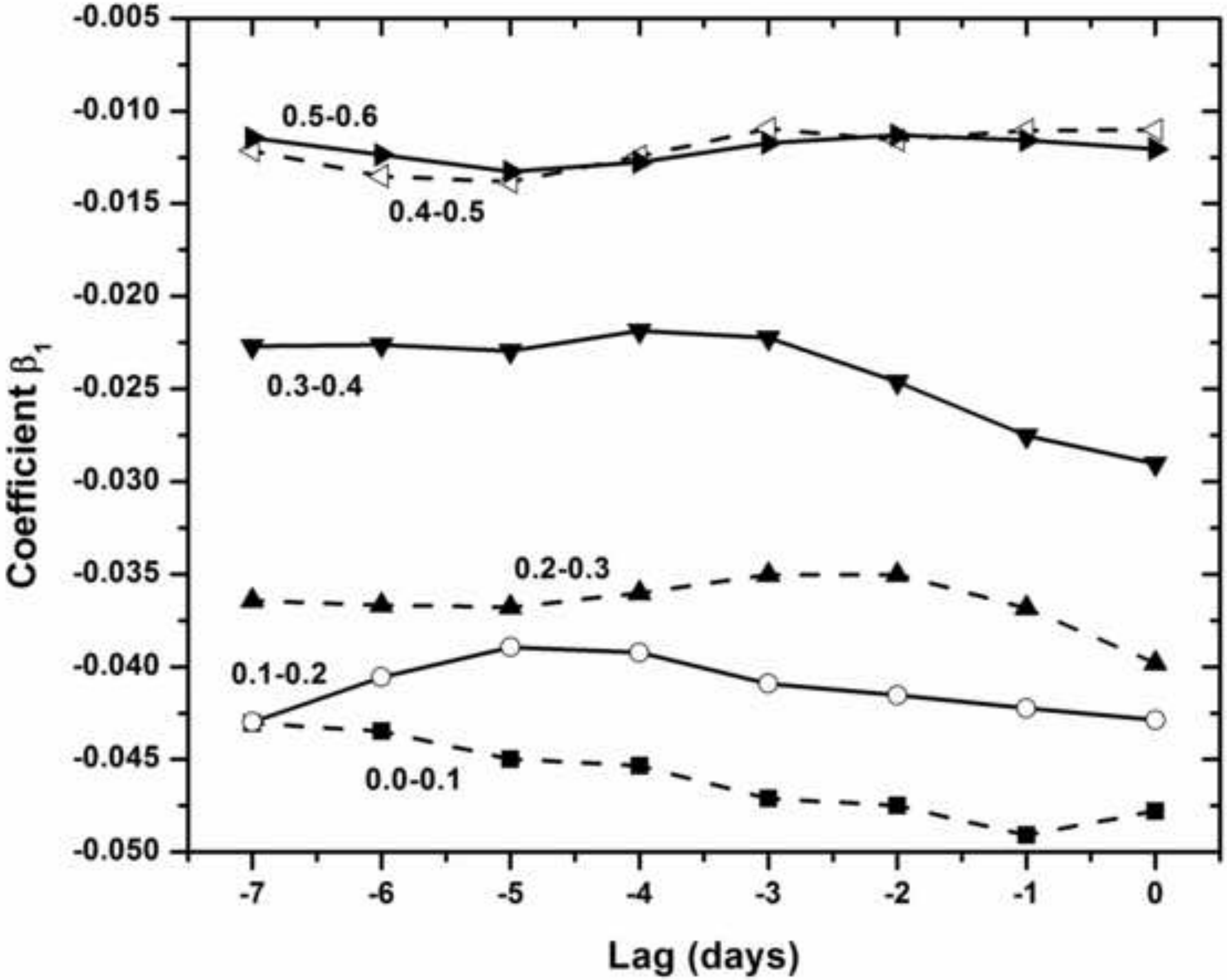
-0.005
-0.010
-0.015
-0.020
-0.025
-0.030
-0.035
-0.040
-0.045
-0.050
Coefficient β1
0.5-0.6
0.4-0.5
0.3-0.4
0.2-0.3
0.1-0.2
0.0-0.1
-7
-6
-5
-4
-3
-2
-1
0
Lag (days)

Figure 12

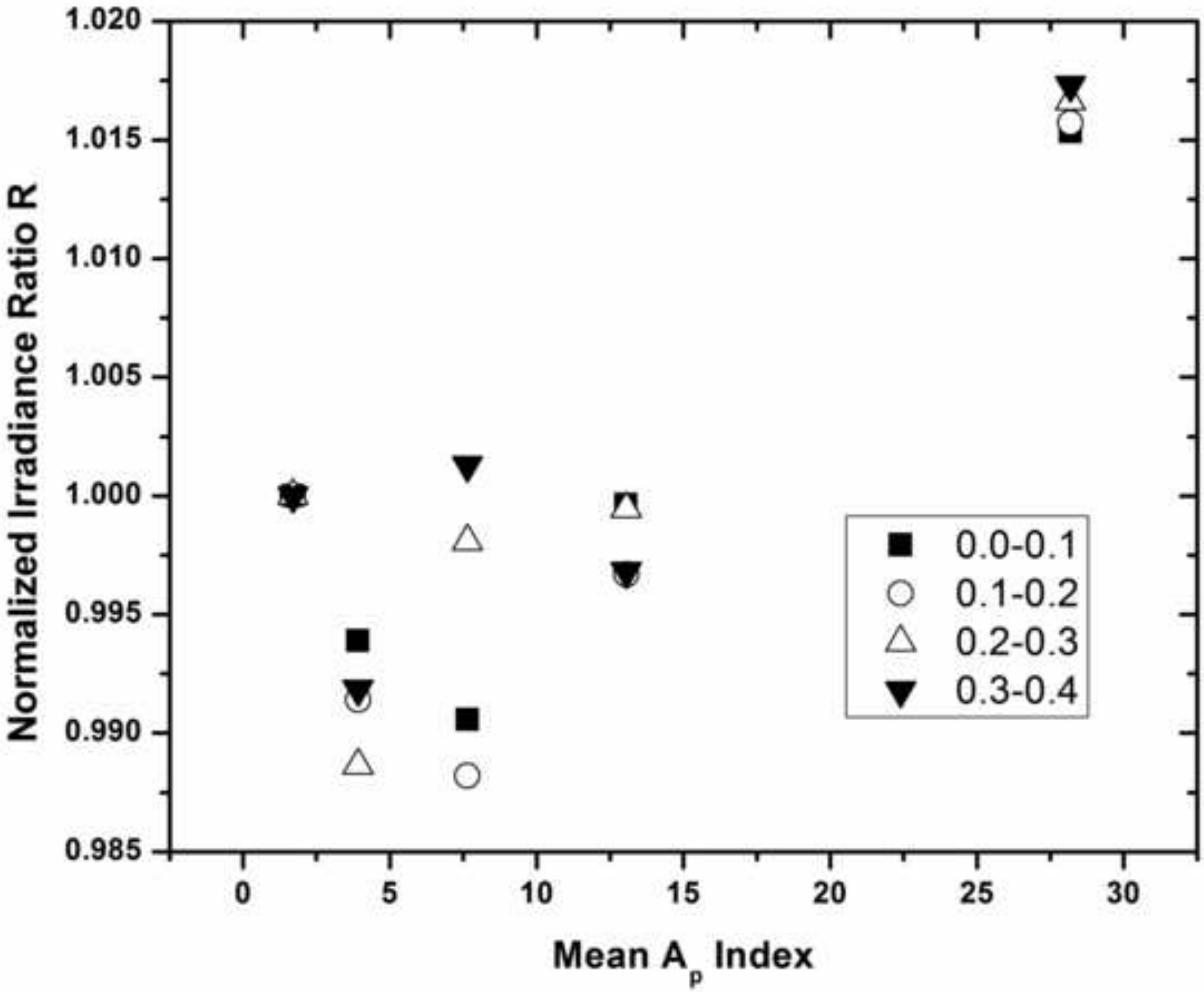

1.020
1.015
1.010
1.005
1.000
0.995
0.990
0.985
Normalized Irradiance Ratio R
0
5
10
15
20
25
30
Mean A_p Index
0.0-0.1
0.1-0.2
0.2-0.3
0.3-0.4

Figure 13

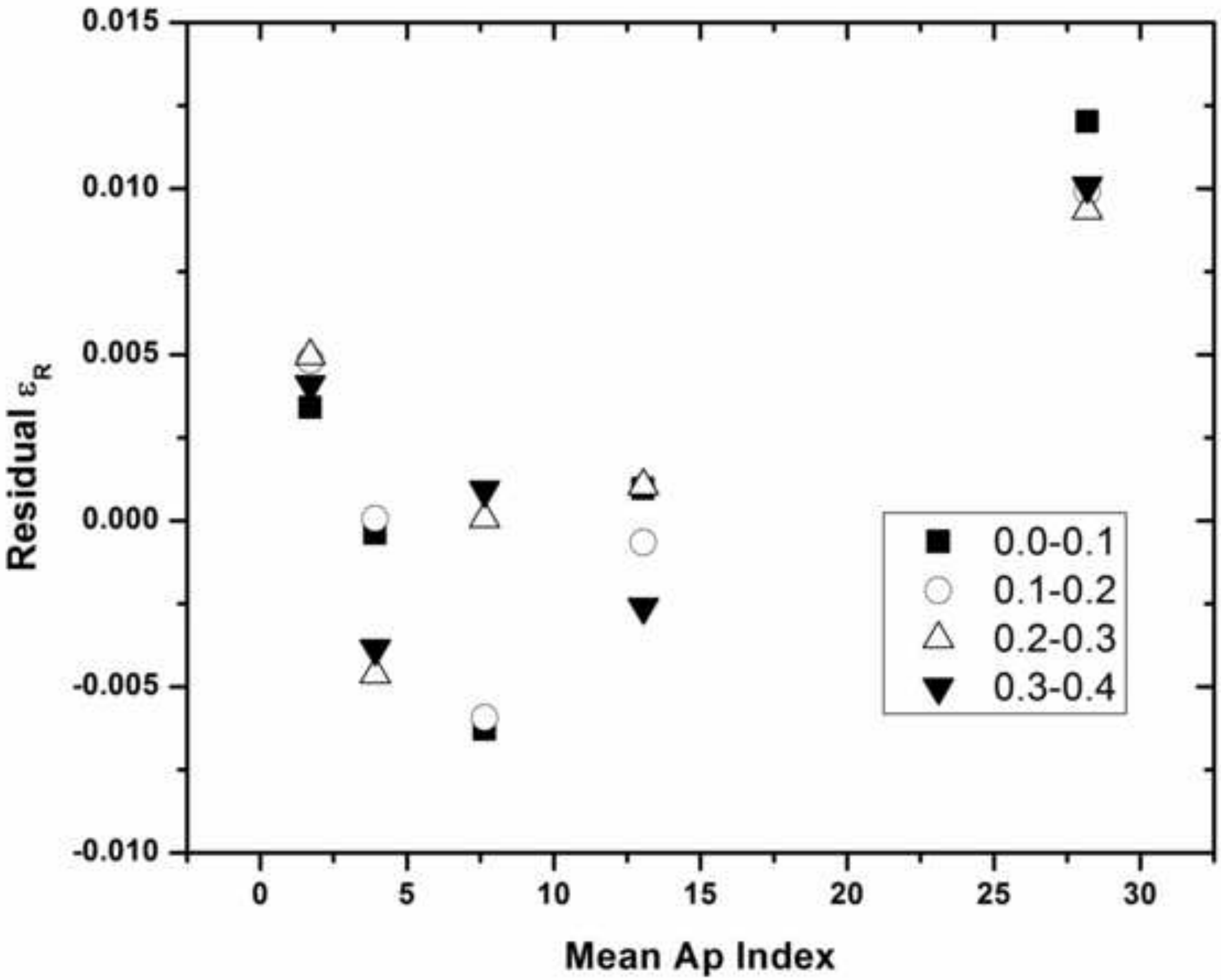

0.015
0.010
0.005
0.000
-0.005
-0.010
Residual ε_R
0
5
10
15
20
25
30
Mean Ap Index
0.0-0.1
0.1-0.2
0.2-0.3
0.3-0.4

Figure 14

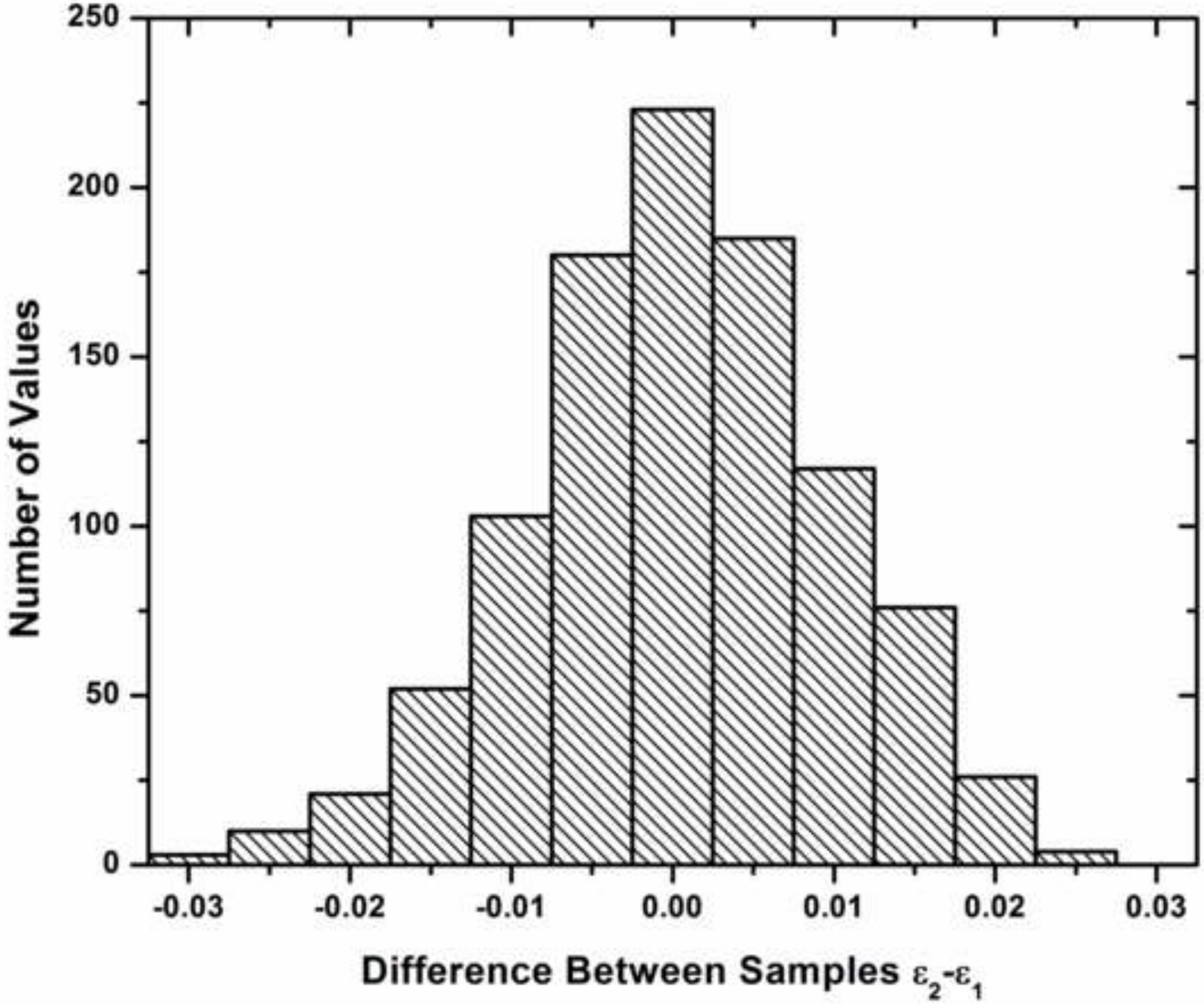

250
200
150
100
50
0
Number of Values
-0.03
-0.02
-0.01
0.00
0.01
0.02
0.03
Difference Between Samples ε2-ε1

Figure 15

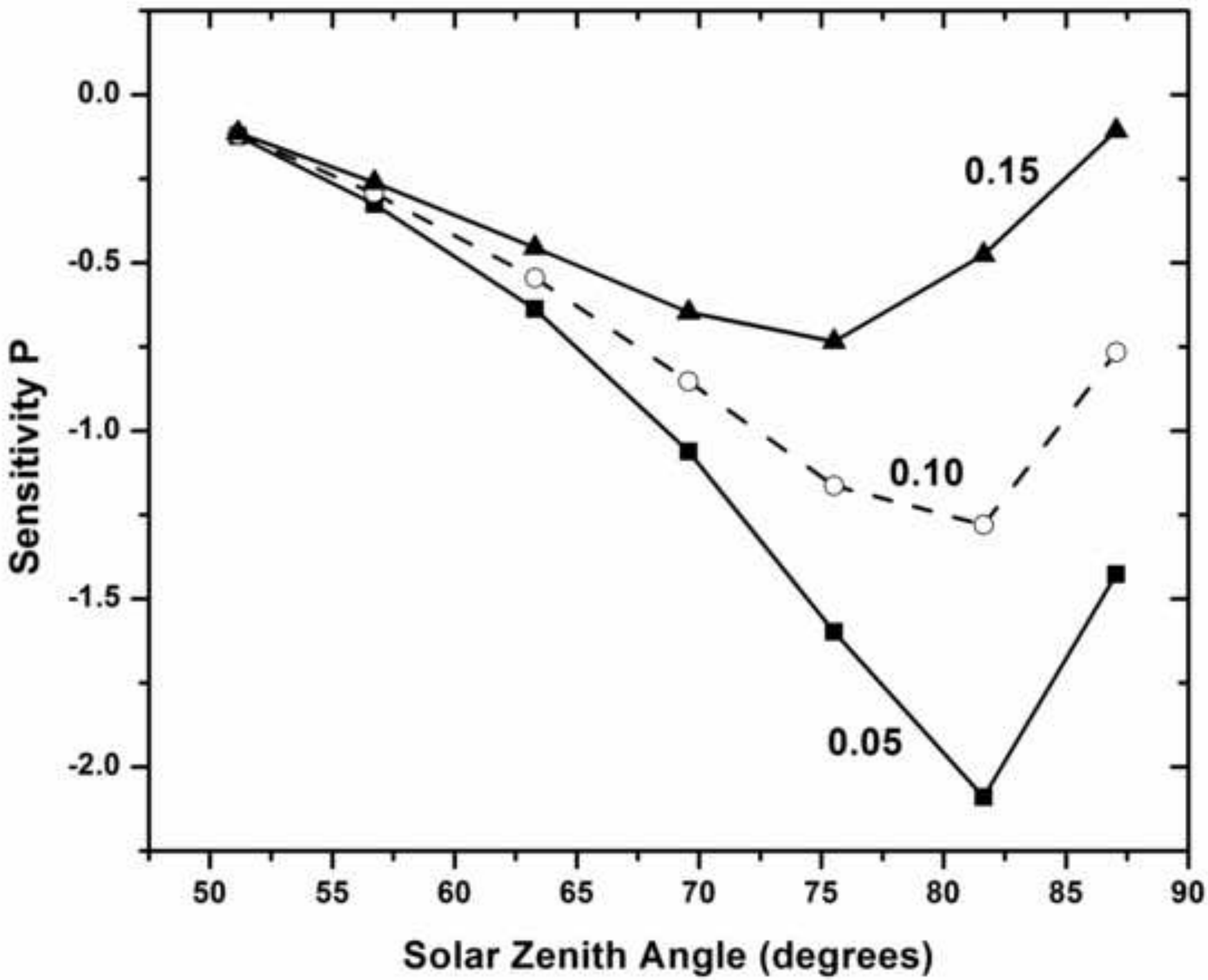

0.0
-0.5
-1.0
-1.5
-2.0
Sensitivity P
50
55
60
65
70
75
80
85
90
Solar Zenith Angle (degrees)
0.15
0.10
0.05

Figure A.1

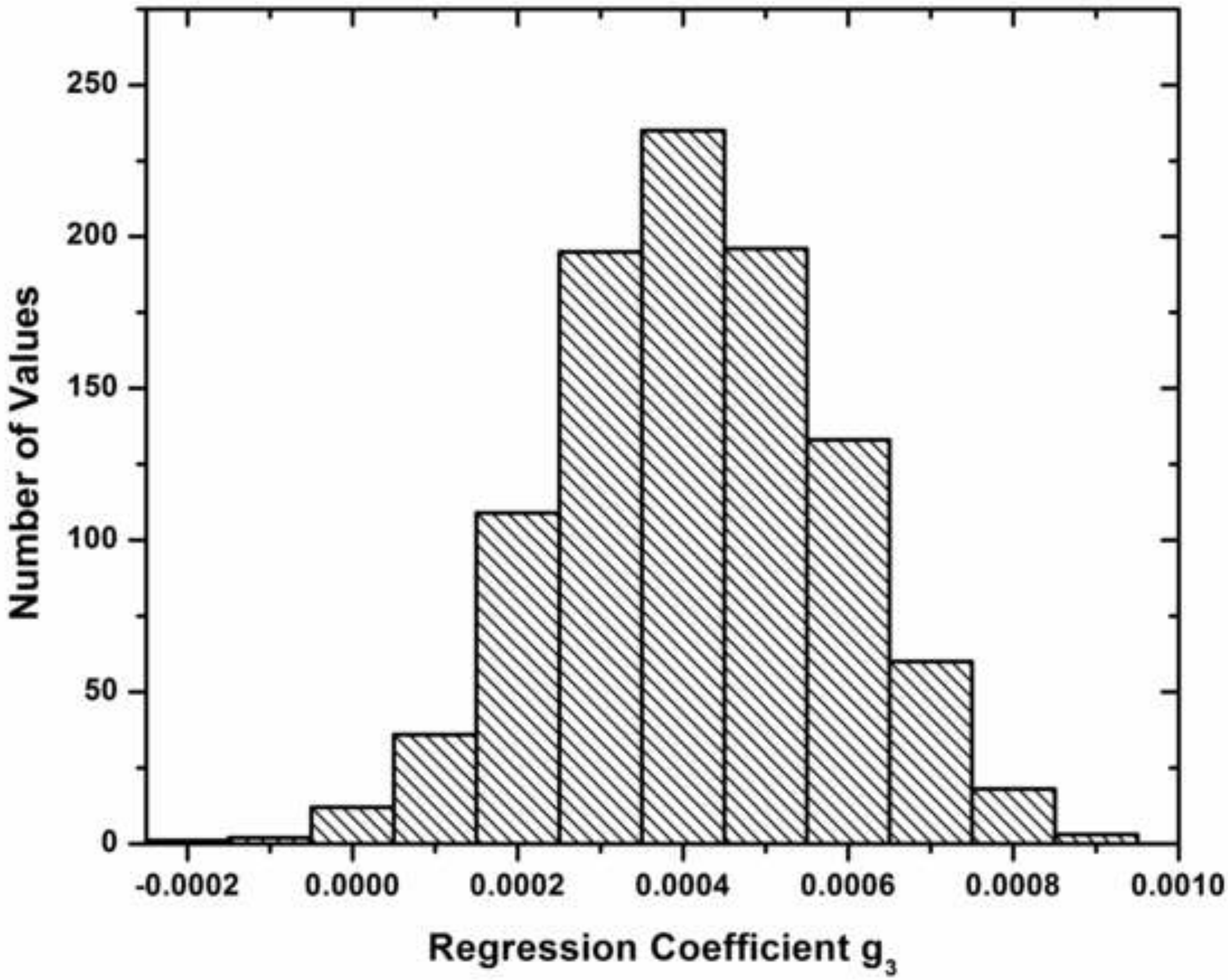
250
200
150
100
50
0
Number of Values
-0.0002
0.0000
0.0002
0.0004
0.0006
0.0008
0.0010
Regression Coefficient g_3

Figure A.2

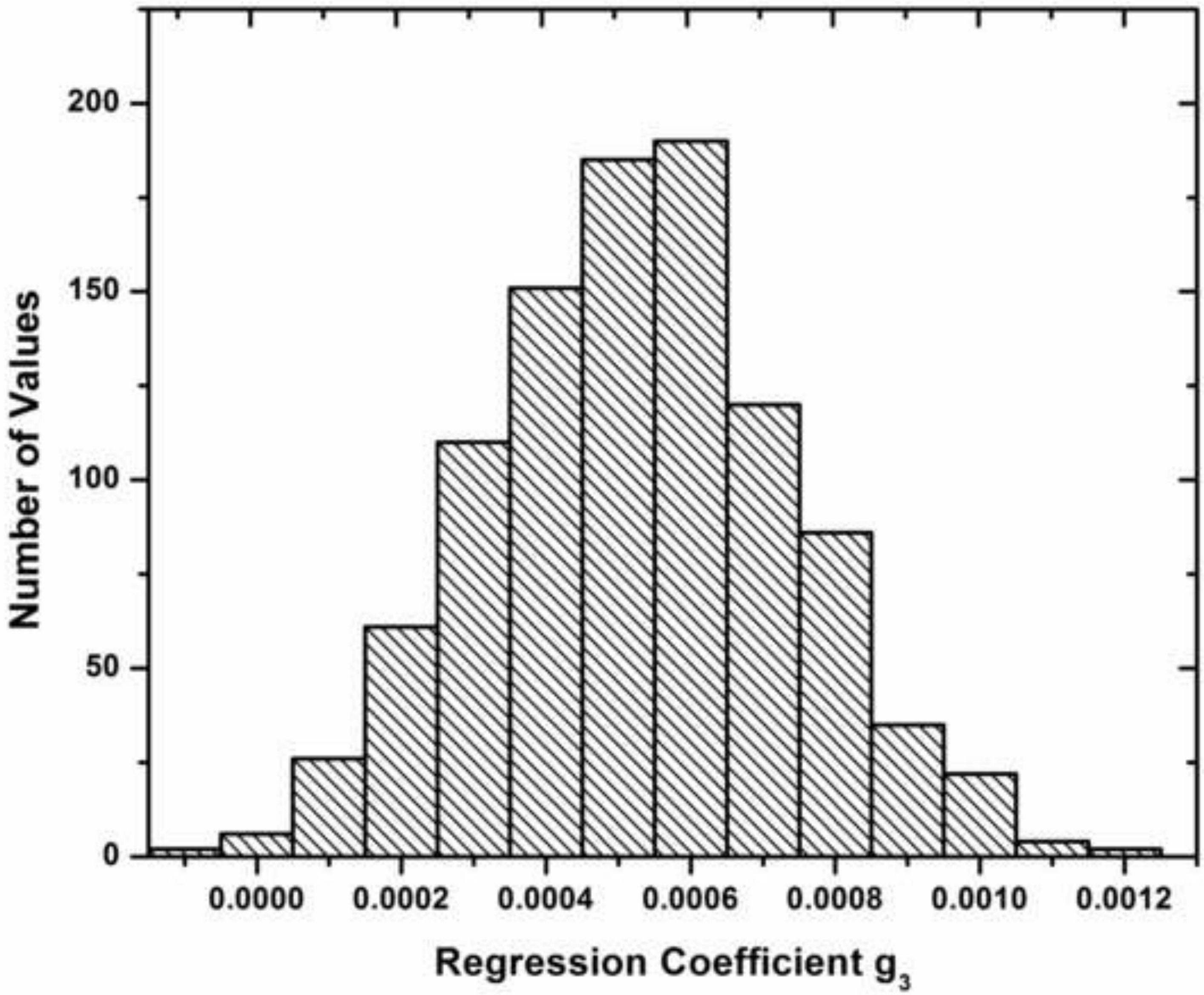

200
150
100
50
0
Number of Values
0.0000
0.0002
0.0004
0.0006
0.0008
0.0010
0.0012
Regression Coefficient g_3